A Distributed Dynamic Load Identification Method Based on the Hierarchical-Clustering-Oriented Radial Basis Function Framework Using Acceleration Signals under Convex-Fuzzy Hybrid Uncertainties

Yaru Liu [a], Min Li [a], Lei Wang [a,b †], Zhangming Wu [b †]

a Institute of Solid Mechanics, School of Aeronautic Science and Engineering, Beihang University, Beijing 100083, China

b School of Engineering, Cardiff University, Newport Road 30-36, CF24 ODE, Cardiff, United Kingdom

[†]Corresponding author: Lei Wang. Email: leiwang_beijing@buaa.edu.cn; ntucee.wanglei@gmail.com

ABSTRACT

Load identification is a hotly studied topic due to the widespread recognition of its importance in structural design and health monitoring. This paper explores an effective identification method for the distributed dynamic load (DDL) varying in both time progress and space dimensions using limited acceleration responses. As for the reconstruction of spatial distribution, the radial basis function (RBF) interpolation strategy, whose hyper-parameters are determined by a hierarchical clustering algorithm, is applied to approximate the DDL and then transform the continuous function into finite dimensions. In the time domain, based on the inverse Newmark iteration, the RBF coefficients at each discrete instant are obtained by the least square solution of the modal forces. Considering the multi-source uncertainties lacking exact probability distributions, a multi-dimensional interval model is developed to quantify convex parameters and fuzzy parameters uniformly. Further, a Chebyshev-interval surrogate model with different orders is constructed to obtain the fuzzy-interval boundaries of DDLs. Eventually, three examples are discussed to demonstrate the feasibility of the developed DDL identification approach considering hybrid uncertainties. The results suggest its promising applications in different structures and loading conditions.

Keywords: distributed dynamic load identification; inverse Newmark iteration; RBF interpolation; hierarchical clustering; convex-fuzzy hybrid uncertainties; Chebyshev-interval method

1 Introduction

Mechanical systems are often subject to distributed dynamic loads (DDLs), such as the aerodynamic load on the aircraft skin and the wind load on the bridge structure [1-3]. Load environment precognition has inspired the development of health monitoring and structural design. There is no denying that the DDL is more complicated than the well-explored one-point/ multi-point concentrated dynamic loads (CDLs), due to the continuity in the time-space dimension. In addition, only limited acceleration responses can be obtained from the perspective of sensor installation, which intensifies the difficulty of DDL identification.

In general, DDL identification is developed on the basis of CDL identification, and the review of CDL identification can reference our previous work [4, 5] and will not be repeated herein. On the one hand, the spatial distribution of DDLs can be approximated by linearly independent basis functions, and then the DDL identification is transformed into coefficients determination of basis functions [6, 7]. Liu et al. [8] provided tailored basis functions to decompose the spatial function of DDLs and the resulting responses, then identified the common weighting coefficients by a Tikhonov regularization scheme. For the flight loads with spatial distribution, Coates et al. [9] selected the most appropriate Fourier coefficient among the pre-developed database by minimizing the error of measured and calculated strains. Based on the orthogonal decomposition, Granger et al. [10], Dessi et al. [11] also developed a series of works on DDL identification. On the other hand, the continuous DDL can be equivalent to several concentrated loads acting on appropriate locations that may induce identical dynamic responses. In view of this, Liu et al. [12] identified concentrated loads sparsely by the combination with blind source separation and orthogonal matching pursuit, however, the results are non-uniqueness.

This work focuses on the first method of DDL identification and aims to establish a universal set of basis functions. Especially, the radial basis function (RBF) has been intensively investigated in the field of data processing and interpolation [13, 14], which can describe the multivariate nonlinear function via one-variable functions (distance function). Any expressions with radial symmetry can be regarded as the kernel function of RBF and the Gaussian function is the most common one [15]. To further improve the approximating accuracy, considerable researches are devoted to parameter selection for kernel functions. In parallel to the RBF neural network with some training samples, some strategies, such as self-organizing learning [16], supervised learning [17] and orthogonal least-squares [18], are

developed concerning the central parameters of hidden layer neurons.

Most previous works on DDL identification were carried out with deterministic assumptions, however, uncertain factors originating from e the static fluctuation (e.g., modeling error and material dispersion) and time-varying factors (e.g., measurement error and signal noises) are often inevitable [19]. These uncertainties can be essentially manifested by their properties of randomness, fuzziness and convexness. For complex systems, different kinds of uncertain information are often encountered simultaneously. Reasonable quantification and propagation treatments of hybrid uncertainties is a precondition for non-deterministic DDL identification. Jiang et al. [20] reviewed the probability-interval hybrid uncertainties from the perspective of uncertainty modeling, uncertainty propagation, structural reliability analysis and reliability-based design optimization. Prasad et al. [21] conducted a Chebyshev-polynomial chaos metamodel for uncertainty analysis for mixed epistemic-aleatory problems caused by imprecise knowledge and random variability in the transmission of line networks. Yin et al. [22] established a hybrid Finite Element/Statistical Energy Analysis model considering fuzzy and interval uncertainties based on first-order perturbation, second-order perturbation and Chebyshev approximation. More excellent researches are illustrated in Ref. [23-25]. However, a unified framework integrating heterogeneous uncertainties was not taken into account in previous studies. Additionanlly, the interval model is usually used to declare the convex uncertainties ignoring the correlation between uncertain parameters.

The problem is solved as follows. In Section 2, the basic formulas of the structural dynamics evolution and RBF interpolation approximation are reviewed. In Section 3, the hierarchical clustering approach is adopted to determine RBF parameters systematically, and the RBF coefficients of DDLs at each instant are subsequently solved based on limited acceleration signals. In Section 4, the quantification and propagation analysis in the context of convex-fuzzy hybrid uncertainties is expounded by the combination of interval modeling and the Chebyshev-interval method. The verification of the proposed methodology is eventually demonstrated by three numerical examples in Section 6. Some conclusions are drawn at the end of the article.

2 Statements of the problem

DDL identification can reconstruct the load tendency in time domain as well as the load distribution in space domain. On the one hand, the dynamic load is discretized into a time

series in time history; on the other hand, its spatial distribution with infinite dimension is transformed into a finite dimension at each time step. In this section, the preparatory works are introduced in consideration of multi-source uncertainties, including the dynamical evolution process and the finite-dimensional approximation.

2.1 Forward analyses of structural dynamics

With regard to a continuous linear system, the rule of uncertain motion can be characterized by the following partial differential equation [26]

$$M(\mathbf{b},\mathbf{L})\frac{\partial^2 w(\mathbf{b},\mathbf{L},t)}{\partial t^2}+\frac{\partial}{\partial t}C(\mathbf{b},\mathbf{L})\Lambda\left[w(\mathbf{b},\mathbf{L},t)\right]+K(\mathbf{b},\mathbf{L})\Psi\left[w(\mathbf{b},\mathbf{L},t)\right]=F(\mathbf{b},\mathbf{L},t) \quad (1)$$

where $\mathbf{b}$ signifies multi-source uncertain parameters vector; t is the time variable and $\mathbf{L}\in\Omega$ is the space variable; $M(\mathbf{b},\mathbf{L})$, $C(\mathbf{b},\mathbf{L})$ and $K(\mathbf{b},\mathbf{L})$ reveal the structural mass, damping and stiffness properties; $w(\mathbf{b},\mathbf{L},t)$ represents the structural displacement function; $F(\mathbf{b},\mathbf{L},t)$ denotes the external DDL function; and $\Lambda\left[w(\mathbf{b},\mathbf{L},t)\right]$, $\Psi\left[w(\mathbf{b},\mathbf{L},t)\right]$ are assigned as differential operators of displacement $w(\mathbf{b},\mathbf{L},t)$ concerning the space variable $\mathbf{L}$. The spatial coordinate system $\Omega\subset\mathbb{R}^{\kappa}$ may describe one-dimensional beams ($\kappa=1$), two-dimensional plates ($\kappa=2$) and three-dimensional solid structures ($\kappa=3$).

In general, Eq. (1) can be discretized into n degrees of freedom (DOFs) through the finite element method (FEM), namely

$$\begin{cases}\mathbf{M}(\mathbf{b})\ddot{\mathbf{u}}(\mathbf{b},t)+\mathbf{C}(\mathbf{b})\dot{\mathbf{u}}(\mathbf{b},t)+\mathbf{K}(\mathbf{b})\mathbf{u}(\mathbf{b},t)=\mathbf{f}(\mathbf{b},t)\\ \dot{\mathbf{u}}(\mathbf{b},0)=\dot{\mathbf{u}}_0\ ,\ \mathbf{u}(\mathbf{b},0)=\mathbf{u}_0\end{cases} \quad (2)$$

in which $\mathbf{M}(\mathbf{b})\in\mathbb{R}^{n\times n}$, $\mathbf{C}(\mathbf{b})\in\mathbb{R}^{n\times n}$ and $\mathbf{K}(\mathbf{b})\in\mathbb{R}^{n\times n}$ means global characteristic matrices of mass, damping and stiffness; $\ddot{\mathbf{u}}(\mathbf{b},t)\in\mathbb{R}^{n\times 1}$, $\dot{\mathbf{u}}(\mathbf{b},t)\in\mathbb{R}^{n\times 1}$ and $\mathbf{u}(\mathbf{b},t)\in\mathbb{R}^{n\times 1}$ stand for the transient response vectors of acceleration, velocity and displacement; $\mathbf{f}(\mathbf{b},t)\in\mathbb{R}^{n\times 1}$ is the load vector discretized by the DDL; $\dot{\mathbf{u}}_0$ and $\mathbf{u}_0$ read corresponding initial conditions, which are always set as 0. Based on the mode superposition theory for classically-damped linear systems, Eq. (2) can be decoupled into a series of differential equations of single-DOF systems. The decoupled r-th ($r=1,2,\cdots,n$) modal equation can be depicted as

$$\begin{cases}\mathbf{M}_q^r(\mathbf{b})\ddot{\mathbf{q}}^r(\mathbf{b},t)+\mathbf{C}_q^r(\mathbf{b})\dot{\mathbf{q}}^r(\mathbf{b},t)+\mathbf{K}_q^r(\mathbf{b})\mathbf{q}^r(\mathbf{b},t)=\mathbf{P}^r(\mathbf{b},t)\\ \dot{\mathbf{q}}^r(\mathbf{b},0)=0\ ,\ \mathbf{q}^r(\mathbf{b},0)=0\end{cases} \quad (3)$$

where $\mathbf{M}_q^r(\mathbf{b})=\boldsymbol{\varphi}_r^T(\mathbf{b})\mathbf{M}(\mathbf{b})\boldsymbol{\varphi}_r(\mathbf{b})$, $\mathbf{C}_q^r(\mathbf{b})=\boldsymbol{\varphi}_r^T(\mathbf{b})\mathbf{C}(\mathbf{b})\boldsymbol{\varphi}_r(\mathbf{b})$ and $\mathbf{K}_q^r(\mathbf{b})=\boldsymbol{\varphi}_r^T(\mathbf{b})\mathbf{K}(\mathbf{b})\boldsymbol{\varphi}_r(\mathbf{b})$ represent the r-th modal mass, damping and stiffness respectively; $\mathbf{q}^r(\mathbf{b},t)$ is the modal

displacement response, and $\mathbf{P}^r(\mathbf{b},t)=\boldsymbol{\varphi}_r^T(\mathbf{b})\mathbf{f}(\mathbf{b},t)$ is the relevant modal force. The modal matrix satisfies $\mathbf{u}(\mathbf{b},t)=\boldsymbol{\Phi}(\mathbf{b})\mathbf{q}(\mathbf{b},t)=\left[\boldsymbol{\varphi}_1(\mathbf{b}),\boldsymbol{\varphi}_2(\mathbf{b}),\cdots,\boldsymbol{\varphi}_n(\mathbf{b})\right]\left[\mathbf{q}^1(\mathbf{b},t),\mathbf{q}^2(\mathbf{b},t),\cdots,\mathbf{q}^n(\mathbf{b},t)\right]^T$. To alleviate the computational burden, the first k-order modes are involved herein. Then, we have $\mathbf{u}(\mathbf{b},t)=\boldsymbol{\Phi}_k(\mathbf{b})\mathbf{q}_k(\mathbf{b},t)=\left[\boldsymbol{\varphi}_1(\mathbf{b}),\boldsymbol{\varphi}_2(\mathbf{b}),\cdots,\boldsymbol{\varphi}_k(\mathbf{b})\right]\left[\mathbf{q}^1(\mathbf{b},t),\mathbf{q}^2(\mathbf{b},t),\cdots,\mathbf{q}^k(\mathbf{b},t)\right]^T$.

In terms of transient-dynamics analysis, the classical Newmark difference scheme is usually employed. Then, the recursive formula for the r-th ($r=1,2,\cdots,k$) modal responses can be detailed by

$$\begin{aligned}\mathbf{q}^r(\mathbf{b},t+\Delta t)&=\mathbf{q}^r(\mathbf{b},t)+\Delta t\dot{\mathbf{q}}^r(\mathbf{b},t)+(1/2-\beta)(\Delta t)^2\ddot{\mathbf{q}}^r(\mathbf{b},t)+\beta(\Delta t)^2\ddot{\mathbf{q}}^r(\mathbf{b},t+\Delta t)\\ \dot{\mathbf{q}}^r(\mathbf{b},t+\Delta t)&=\dot{\mathbf{q}}^r(\mathbf{b},t)+(1-\gamma)\Delta t\ddot{\mathbf{q}}^r(\mathbf{b},t)+\gamma\Delta t\ddot{\mathbf{q}}^r(\mathbf{b},t+\Delta t)\end{aligned} \tag{4}$$

where $\Delta t=T/S$ is time increment. T and S are loading duration and total steps. γ and β is set as control parameters of the Newmark scheme [2]. Substituting the differential equations at time t and $t+\Delta t$ into Eq. (4), it yields

$$\mathbf{K}^{*r}(\mathbf{b})\mathbf{q}^r(\mathbf{b},t+\Delta t)=\mathbf{P}^r(\mathbf{b},t+\Delta t)+\mathbf{F}^{*r}(\mathbf{b},t) \tag{5}$$

where

$$\begin{aligned}\mathbf{K}^{*r}(\mathbf{b})&=\frac{1}{\beta(\Delta t)^2}\mathbf{M}_q^r(\mathbf{b})+\frac{\gamma}{\beta\Delta t}\mathbf{C}_q^r(\mathbf{b})+\mathbf{K}_q^r(\mathbf{b})\\ \mathbf{F}^{*r}(\mathbf{b},t)&=\mathbf{M}_q^r(\mathbf{b})\left[\frac{1}{\beta(\Delta t)^2}\mathbf{q}^r(\mathbf{b},t)+\frac{1}{\beta\Delta t}\dot{\mathbf{q}}^r(\mathbf{b},t)+\left(\frac{1}{2\beta}-1\right)\ddot{\mathbf{q}}^r(\mathbf{b},t)\right]+\\ &\quad\mathbf{C}_q^r(\mathbf{b})\left[\frac{\gamma}{\beta\Delta t}\mathbf{q}^r(\mathbf{b},t)+\left(\frac{\gamma}{\beta}-1\right)\dot{\mathbf{q}}^r(\mathbf{b},t)+\left(\frac{\gamma}{2\beta}-1\right)\ddot{\mathbf{q}}^r(\mathbf{b},t)\right]\end{aligned} \tag{6}$$

Under such circumstances, the modal displacement response $\mathbf{q}^r(\mathbf{b},t+\Delta t)$ can be considered as a superposition of two components, i.e., $\mathbf{q}^r(\mathbf{b},t+\Delta t)=\mathbf{q}_1^r(\mathbf{b},t+\Delta t)+\mathbf{q}_2^r(\mathbf{b},t+\Delta t)$. $\mathbf{q}_1^r(\mathbf{b},t+\Delta t)$ is caused by the modal load $\mathbf{P}^r(\mathbf{b},t+\Delta t)$ at instant $t+\Delta t$ and $\mathbf{q}_2^r(\mathbf{b},t+\Delta t)$ by the combination of modal responses $\mathbf{F}^{*r}(\mathbf{b},t)$ at instant t.

2.2 RBF interpolation techniques for DDL approximation

The transformation of discrete measurements into continuously distributed loads can be achieved by data interpolation or fitting. Due to the unknown features of DDLs, there is an urgent need to find an efficient method for both smooth and strongly nonlinear functions. In particular, the RBF interpolation [13] incorporates linear and non-linear basis functions, then the non-linear correlations in low-dimensional spaces may be converted into linear when projected onto higher-dimensional spaces by the RBF. Thus, the RBF interpolation is applied to match the spatial distribution of the DDL herein. Given a set $\mathbf{X}=\left\{\mathbf{x}_1,\mathbf{x}_2,\cdots,\mathbf{x}_q\right\}\subset\mathbb{R}^\kappa$ in

space Ω, the function $F(\mathbf{b},\mathbf{L},t)$ can be written as

$$F(\mathbf{b},\mathbf{L},t)=\sum_{j=1}^{q}\alpha_j(\mathbf{b},t)\phi(\left\|\mathbf{L}-\mathbf{x}_j\right\|)+\sum_{h=0}^{\kappa}\eta_h(\mathbf{b},t)\,p_h(\mathbf{L}) \tag{7}$$

where $\mathbf{X}$ is called the center set; ϕ is a nonlinear basis function; $\left\|\mathbf{L}-\mathbf{x}_j\right\|$ ($j=1,2,\cdots,q$) denotes the Euclidean distance between $\mathbf{L}$ and $\mathbf{x}_j$; $p_h(\mathbf{L})$ ($h=0,\cdots,\kappa$) is a component of linear polynomial basis to ensure the non-singularity of the subsequent coefficient solution; $\alpha_j(\mathbf{b},t)$ and $\eta_h(\mathbf{b},t)$ are the corresponding undetermined coefficients. It is noted that as long as the elements within $\mathbf{X}$ are different from each other, the function $\left\{\phi(\left\|\mathbf{L}-\mathbf{x}_j\right\|)\right\}$ will be linearly independent. In addition, the RBF coefficients and polynomial basis should obey the orthogonality conditions, i.e.,

$$\sum_{j=1}^{q}\alpha_j(\mathbf{b},t)\,p_h(\mathbf{x}_j)=0 \quad , \quad h=0,1,\cdots,\kappa \tag{8}$$

There are many specific functional forms available in the literature for the nonlinear basis function. In this work, without loss of generality, the Gaussian function is used as the nonlinear basis function, which can be expressed as

$$\phi(\left\|\mathbf{L}-\mathbf{x}_j\right\|)=\exp\left(-\frac{1}{2\sigma_j^{\,2}}\left\|\mathbf{L}-\mathbf{x}_j\right\|^2\right) \tag{9}$$

where σ_j is the variance of the Gaussian function, which controls its width. The value of $\phi(\left\|\mathbf{L}-\mathbf{x}_j\right\|)$ increases as the distance $\left\|\mathbf{L}-\mathbf{x}_j\right\|$ decreases. To better control its action scope, the spatial coordinate $\mathbf{L}$ is recommended to be regularized to a standard interval as follows

$$\tilde{\mathbf{L}}^i=\frac{2\mathbf{L}^i-\left(A_{\max}+A_{\min}\right)}{A_{\max}-A_{\min}} \quad , \quad i=1,\cdots,\kappa \tag{10}$$

where $\mathbf{L}^i$ and $\tilde{\mathbf{L}}^i$ are the original coordinate and the regularized coordinate in the i-th dimension. $\left[A_{\min},A_{\max}\right]$ is the standard interval. Then Eq. (7) will be transformed as

$$F(\mathbf{b},\mathbf{L},t)\to F(\mathbf{b},\tilde{\mathbf{L}},t)=\sum_{j=1}^{q}\alpha_j(\mathbf{b},t)\phi(\left\|\tilde{\mathbf{L}}-\mathbf{x}_j\right\|)+\sum_{h=0}^{\kappa}\eta_h(\mathbf{b},t)\,p_h(\tilde{\mathbf{L}}) \tag{11}$$

To gain more insight, the Euclidean distance, linear polynomial basis and orthogonality conditions of the three-dimensional solid structure can be defined as

$$\begin{gathered}\left\|\tilde{\mathbf{L}}-\mathbf{x}_j\right\|=\sqrt{(\tilde{x}-x_j)^2+(\tilde{y}-y_j)^2+(\tilde{z}-z_j)^2}\\ p(\mathbf{b},\mathbf{L},t)=\eta_0(\mathbf{b},t)+\eta_1(\mathbf{b},t)\tilde{x}+\eta_2(\mathbf{b},t)\tilde{y}+\eta_3(\mathbf{b},t)\tilde{z}\\ \sum_{j=1}^{q}\alpha_j(\mathbf{b},t)=\sum_{j=1}^{q}\alpha_j(\mathbf{b},t)x_j=\sum_{j=1}^{q}\alpha_j(\mathbf{b},t)y_j=\sum_{j=1}^{q}\alpha_j(\mathbf{b},t)z_j=0\end{gathered} \tag{12}$$

where x_j, y_j and z_j are coordinates of the center $\mathbf{x}_j$. Fig. 1 shows the RBF interpolation scheme for one-dimensional and two-dimensional situations, in which any curves or surfaces can be approximated once the RBF center is determined. In addition, the RBF interpolation is not the unique choice; other models such as polynomial interpolation, spline function interpolation, Kriging interpolation can be used for DDL spatial discretization.

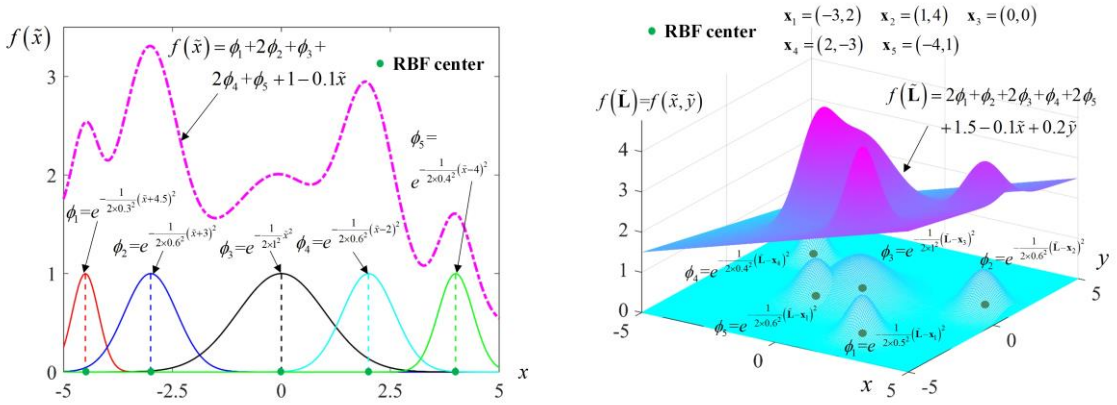

(a) One-dimensional approximation (b) Two-dimensional approximation

Fig. 1 The distributed function approximation by RBF

3 DDL identification via hierarchical clustering and acceleration signals

It is generally accepted that the computational complexity and approximating precision depend on the dispersion of the center set $\mathbf{X}$ and its number q. In addition, the shape of $\phi(\|\tilde{\mathbf{L}}-\mathbf{x}_j\|)$ is determined by the parameter σ_j. How to determine the hyper-parameters of the RBF approximation and then inverse the coefficients $\alpha_j(\mathbf{b},t)$, ($j=1,2\cdots,q$) and $p_h(\mathbf{L})$ ($h=0,1,\cdots,\kappa$) through accessible acceleration signals are discussed in this section.

3.1 RBF determinations by hierarchical clustering

Given that the DDLs on FEM nodes are related to spatial locations, the normalized coordinates $\tilde{\mathbf{L}}_{surface}=\{\tilde{\mathbf{L}}_1,\tilde{\mathbf{L}}_2,\cdots,\tilde{\mathbf{L}}_m\}\subset\mathbb{R}^{\kappa}(\kappa=1,2,3)$ with m samples may be introduced to determine the overall arrangement of RBF approximation. As mentioned in the introduction section, several approaches have been developed for the determination of the RBF centers. In general, the center is chosen at random and the width is determined by experience, which is more demanding in terms of node coordinates and is only applicable if the selected centers are representative. Subsequently, self-organizing learning methods based on K-means clustering [27] were developed with the given initial cluster center. However, the number q should be specified in advance and clustering results maybe not be assigned as unique. In

order to overcome the difficulties of large randomness, slow convergence and strong initial dependence, the hierarchical clustering algorithm [28] is incorporated herein and the specific process is as follows.

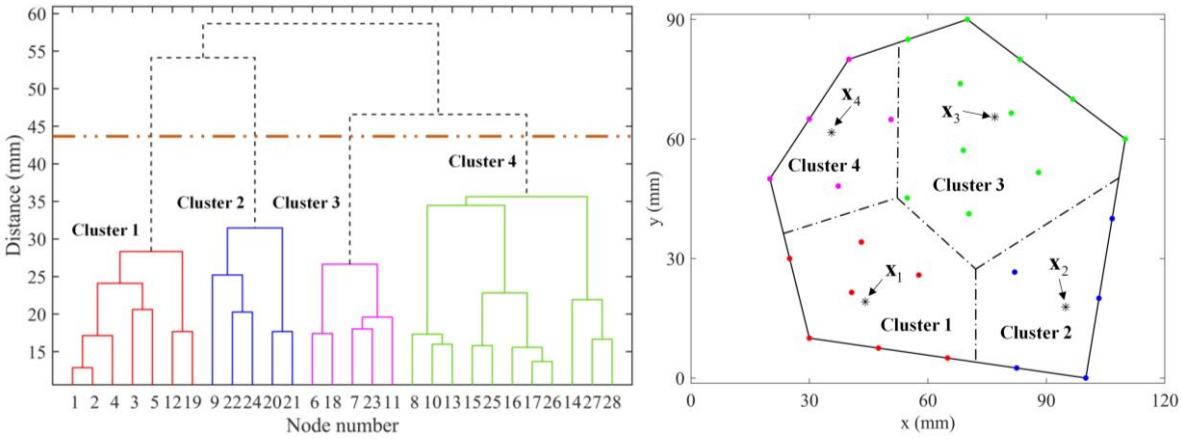

(a) The dendrogram (b) Hierarchical clustering results

Fig. 2 Schematic diagram of hierarchical clustering

Compared with the RBF neural network, the normalized coordinates $\tilde{\mathbf{L}}_{surface}$ are equivalent to the training samples of the input layer, and the center set $\mathbf{X}$ is equivalent to the neuron center of the hidden layer. By virtue of the hierarchical clustering algorithm, every sample of $\tilde{\mathbf{L}}_{surface}$ is regarded as an initial cluster to produce m clusters firstly. Then the two clusters with the nearest distance may be merged continually until the m samples are integrated into one cluster. The key of this algorithm is to calculate the between-cluster distance. Let ξ_{vw} represent the distance between the sample $\tilde{\mathbf{L}}_v$ and $\tilde{\mathbf{L}}_w$, which can be calculated by the Euclidean distance, namely

$$\xi_{vw} = \left\| \tilde{\mathbf{L}}_v^i - \tilde{\mathbf{L}}_w^i \right\| = \sqrt{\sum_{i=1}^{\kappa} \left(\tilde{\mathbf{L}}_v^i - \tilde{\mathbf{L}}_w^i \right)^2} \tag{13}$$

Let ζ_{po} is the distance between cluster E_p and cluster E_o. Considering the information of all samples in a cluster, the average-linkage between-cluster distance [29] can be given by

$$\zeta_{po} = \frac{1}{\Delta_p \Delta_o} \sum_{\tilde{\mathbf{L}}_v \in \mathrm{E}_p} \sum_{\tilde{\mathbf{L}}_w \in \mathrm{E}_o} \xi_{vw} \tag{14}$$

where Δ_p and Δ_o are sample sizes. When the cluster E_p and cluster E_o are merged into a new cluster E_a, the distance between cluster E_a and another cluster E_e can be given by

$$\zeta_{ae} = \frac{1}{\Delta_a \Delta_e} \sum_{\tilde{\mathbf{L}}_v \in \mathrm{E}_a} \sum_{\tilde{\mathbf{L}}_w \in \mathrm{E}_e} \xi_{vw} = \frac{\Delta_p}{\Delta_a} \zeta_{pe} + \frac{\Delta_o}{\Delta_a} \zeta_{oe} \tag{15}$$

The number of generated clusters in the hierarchical clustering process is settled as the

centers' number q. The maximum between-cluster distance, namely, the merging distance ζ^{m-1} at the last step, is employed to determine the value of q. Suppose that the merging distance in the ε-th iteration is $\zeta^{(\varepsilon)}$. It indicates the distance is large enough and the similarity is small enough between any two clusters if $\zeta^{(\varepsilon)} \geq \tau\zeta^{m-1}$ (τ is the proportional coefficient). Accordingly, the normalized coordinates of FEM nodes are divided into $q = m - \varepsilon$ clusters ($\left\{\widehat{\mathrm{E}}_1, \widehat{\mathrm{E}}_2, \cdots, \widehat{\mathrm{E}}_{m-\varepsilon}\right\}$). An irregular hexagon with 18 nodes is taken as an example to illustrate the entire clustering procedure, whose dendrogram is plotted in Fig. 2 (a). Segmenting the clustering results with the double dots line, 4 clusters are created as shown in Fig. 2 (b). Once q is determined, the j-th center $\mathbf{x}_j$ can be obtained by the ultimate cluster $\widehat{\mathrm{E}}_j$ as follows

$$\mathbf{x}_j = \frac{1}{\Delta_j} \sum_{\tilde{\mathbf{L}}_* \in \widehat{\mathrm{E}}_j} \tilde{\mathbf{L}}_* \quad , \quad j = 1, 2, \cdots m - \varepsilon \tag{16}$$

Eventually, the variance σ_j of the nonlinear basis function $\phi(\left\|\mathbf{L} - \mathbf{x}_j\right\|)$ can be given by

$$\sigma_j = \lambda \Im_j \quad , \quad \Im_j = \min\left(\left\|\mathbf{x}_j - \mathbf{x}_i\right\|\right) \tag{17}$$

where $\Im_j$ is the minimum distance between the j-th center $\mathbf{x}_j$ and another center $\mathbf{x}_i$ ($i = 1, 2, \cdots, q$ but $i \neq j$). λ is the overlap coefficient, which reflects the smoothness of the function $\phi(\left\|\tilde{\mathbf{L}} - \mathbf{x}_j\right\|)$. Moreover, the larger the λ is, the smoother the $\phi(\left\|\tilde{\mathbf{L}} - \mathbf{x}_j\right\|)$ is.

To conclude, the hyper-parameters of RBF approximation can be handled by merging clusters reasonably based on the hierarchical-clustering-oriented framework. The RBF centers can be uniquely determined, independent of engineering experiences and initial designs. And a widely applicable RBF space may be constructed eventually by adjusting the proportional coefficient τ and the overlap coefficient λ.

3.2 Coefficient calculations via acceleration signals

As mentioned in section 2.1, the dynamic responses can be deduced iteratively via Eq. (3) -(6) for the forward FEM analyses. In contrast, the external load can also be solved step by step for the inverse problem. However, the accelerometers are often restricted that cannot cover all DOFs. When the time sequence of acceleration signals of G measuring points is provided, the first k-order modal acceleration responses can be calculated by

$$\begin{bmatrix} \ddot{\mathbf{q}}^1(\mathbf{b}, t) \\ \ddot{\mathbf{q}}^2(\mathbf{b}, t) \\ \vdots \\ \ddot{\mathbf{q}}^k(\mathbf{b}, t) \end{bmatrix} = \begin{bmatrix} \boldsymbol{\varphi}_1^{N_1}(\mathbf{b}) & \boldsymbol{\varphi}_2^{N_1}(\mathbf{b}) & \cdots & \boldsymbol{\varphi}_k^{N_1}(\mathbf{b}) \\ \boldsymbol{\varphi}_1^{N_2}(\mathbf{b}) & \boldsymbol{\varphi}_2^{N_2}(\mathbf{b}) & \cdots & \boldsymbol{\varphi}_k^{N_2}(\mathbf{b}) \\ \vdots & \vdots & \ddots & \vdots \\ \boldsymbol{\varphi}_1^{N_G}(\mathbf{b}) & \boldsymbol{\varphi}_2^{N_G}(\mathbf{b}) & \cdots & \boldsymbol{\varphi}_k^{N_G}(\mathbf{b}) \end{bmatrix}^+ \begin{bmatrix} \ddot{\mathbf{u}}_1(t) \\ \ddot{\mathbf{u}}_2(t) \\ \vdots \\ \ddot{\mathbf{u}}_m(t) \end{bmatrix} \Rightarrow \ddot{\mathbf{q}}(\mathbf{b}, t) = \left[\boldsymbol{\Phi}_k(\mathbf{b})\right]^+ \ddot{\mathbf{u}}(t) \tag{18}$$

where $[*]^{+}$ means the Moore-Penrose pseudo inverse operation of $*$; N_i ($i=1,2,\cdots,G$) denotes the DOF of the i-th measuring point; and $\boldsymbol{\varphi}_j^{N_i}(\mathbf{b})$ ($i=1,2,\cdots,G$, j=1,2,$\cdots,k$) represents the value of the j-th natural mode on the i-th DOF. Furthermore, the modal displacement/velocity sequence can be calculated through the Newmark iteration as Eq. (4), and the modal displacement component $\mathbf{q}_2^r(\mathbf{b},t+\Delta t)$ can be calculated through Eq. (6). Another displacement component can be given by $\mathbf{q}_1^r(\mathbf{b},t+\Delta t)=\mathbf{q}^r(\mathbf{b},t+\Delta t)-\mathbf{q}_2^r(\mathbf{b},t+\Delta t)$. Then, the r-th modal force $\mathbf{P}^r(\mathbf{b},t+\Delta t)$ can be analyzed by

$$\mathbf{P}^r(\mathbf{b},t+\Delta t)=\mathbf{K}^{*r}(\mathbf{b})\mathbf{q}_1^r(\mathbf{b},t+\Delta t) \tag{19}$$

With the aid of RBF approximation, the DDF on the v-th FEM node may be written as

$$\mathbf{f}^v(\mathbf{b},t)=F(\mathbf{b},\mathbf{L}_v,t)=\boldsymbol{\Xi}(\tilde{\mathbf{L}}_v)\boldsymbol{\chi}(\mathbf{b},t) \tag{20}$$

where $\tilde{\mathbf{L}}_v$ is the normalized spatial coordinates of the v-th node; $\boldsymbol{\Xi}(\tilde{\mathbf{L}}_v)$ is the basis vector; and $\boldsymbol{\chi}(\mathbf{b},t)$ is the undetermined coefficient vector. They can be detailed as

$$\begin{aligned}\boldsymbol{\Xi}(\tilde{\mathbf{L}}_v)&=\left[\phi(\left\|\tilde{\mathbf{L}}_v-\mathbf{x}_1\right\|)\quad\cdots\quad\phi(\left\|\tilde{\mathbf{L}}_v-\mathbf{x}_q\right\|)\quad p_0(\tilde{\mathbf{L}}_v)\quad\cdots\quad p_\kappa(\tilde{\mathbf{L}}_v)\right]\\ \boldsymbol{\chi}(\mathbf{b},t)&=\left[\alpha_1(\mathbf{b},t)\quad\cdots\quad\alpha_q(\mathbf{b},t)\quad\eta_0(\mathbf{b},t)\quad\cdots\quad\eta_\kappa(\mathbf{b},t)\right]^T\end{aligned} \tag{21}$$

Further, the modal force can be expressed as

$$\begin{aligned}\begin{bmatrix}\mathbf{P}^1(\mathbf{b},t)\\ \mathbf{P}^2(\mathbf{b},t)\\ \vdots\\ \mathbf{P}^k(\mathbf{b},t)\end{bmatrix}&=\begin{bmatrix}\boldsymbol{\varphi}_1^1(\mathbf{b}) & \boldsymbol{\varphi}_2^1(\mathbf{b}) & \cdots & \boldsymbol{\varphi}_k^1(\mathbf{b})\\ \boldsymbol{\varphi}_1^2(\mathbf{b}) & \boldsymbol{\varphi}_2^2(\mathbf{b}) & \cdots & \boldsymbol{\varphi}_k^2(\mathbf{b})\\ \vdots & \vdots & \ddots & \vdots\\ \boldsymbol{\varphi}_1^n(\mathbf{b}) & \boldsymbol{\varphi}_2^n(\mathbf{b}) & \cdots & \boldsymbol{\varphi}_k^n(\mathbf{b})\end{bmatrix}^T\mathbf{T}_f\begin{bmatrix}\boldsymbol{\Xi}(\tilde{\mathbf{L}}_1)\\ \boldsymbol{\Xi}(\tilde{\mathbf{L}}_2)\\ \vdots\\ \boldsymbol{\Xi}(\tilde{\mathbf{L}}_m)\end{bmatrix}\boldsymbol{\chi}(\mathbf{b},t)\\ &\Rightarrow\mathbf{P}(\mathbf{b},t)=\boldsymbol{\Phi}_k^T(\mathbf{b})\mathbf{T}_f\boldsymbol{\Psi}(\tilde{\mathbf{L}})\boldsymbol{\chi}(\mathbf{b},t)\end{aligned} \tag{22}$$

where $\left(\mathbf{T}_f\right)_{n\times m}$ corresponds to the force action matrix composed of 1 and 0. Considering the orthogonality condition of RBF interpolation, Eq. (8) can be rewritten as

$$\begin{bmatrix}p_0(\mathbf{x}_1) & \cdots & p_0(\mathbf{x}_q) & 0 & \cdots & 0\\ \vdots & \ddots & \vdots & \vdots & \ddots & \vdots\\ p_M(\mathbf{x}_1) & \cdots & p_M(\mathbf{x}_q) & 0 & \cdots & 0\end{bmatrix}\boldsymbol{\chi}(\mathbf{b},t)=\begin{bmatrix}0\\ \vdots\\ 0\end{bmatrix}\Rightarrow\ \boldsymbol{\Gamma}(\mathbf{X})\boldsymbol{\chi}(\mathbf{b},t)=\left[\mathbf{0}\right] \tag{23}$$

Combining Eq. (22)-(23), the coefficient vector including $\alpha_j(\mathbf{b},t)$ ($j=1,2,\cdots,q$) and $\eta_h(\mathbf{b},t)$ ($h=0,1,\cdots,\kappa$) at each discrete time can be determined through the least square method, namely

$$\boldsymbol{\chi}(\mathbf{b},t)=\left\{\begin{bmatrix}\boldsymbol{\Phi}_k^T(\mathbf{b})\mathbf{T}_f\boldsymbol{\Psi}(\tilde{\mathbf{L}})\\ \boldsymbol{\Gamma}(\mathbf{X})\end{bmatrix}^T\begin{bmatrix}\boldsymbol{\Phi}_k^T(\mathbf{b})\mathbf{T}_f\boldsymbol{\Psi}(\tilde{\mathbf{L}})\\ \boldsymbol{\Gamma}(\mathbf{X})\end{bmatrix}\right\}^{-1}\begin{bmatrix}\boldsymbol{\Phi}_k^T(\mathbf{b})\mathbf{T}_f\boldsymbol{\Psi}(\tilde{\mathbf{L}})\\ \boldsymbol{\Gamma}(\mathbf{X})\end{bmatrix}^T\begin{bmatrix}\mathbf{P}(\mathbf{b},t)\\ \mathbf{0}\end{bmatrix} \tag{24}$$

4 Uncertainty treatments for the prediction of DDL boundary

The identified DDL may be indeterminate considering the transmissibility of multi-source uncertainties through the convolution relationship between the external DDL and input variables. How to quantitatively describe and effectively propagate uncertain parameters is at the heart of the uncertainty-oriented DDL identification scheme. Frankly speaking, there are three methods to quantify the uncertainties in practical engineering, namely probabilistic model, fuzzy model and convex model. Although the probabilistic approach is most widely used based on classical probability theory and statistical techniques, it is often challenging to obtain exact probability distributions of uncertain variables through limited samples [30]. On the contrary, the membership function for the fuzzy model, and the boundary rules and linear correlation feature for the convex model are relatively easy to be confirmed via engineering experience [31]. That's to say, as an effective complement to the probabilistic model, convex and fuzzy models are more advantageous in dealing with practical problems in information-poor and data-poor situations. Hence, hybrid uncertainties are characterized and further analyzed based on the convex set and fuzzy set in this section.

4.1 Interval modeling of multi-dimensional convex-fuzzy hybrid uncertainties

Once the scatter of uncertainty data of convex uncertainties is obtainable, all possible values $\mathbf{b}_C=\{\mathbf{b}_{C1},\mathbf{b}_{C2},\cdots\mathbf{b}_{CP}\}$ are assumed to be bounded in the multidimensional ellipsoid model $E_{\mathbf{b}_C}$, which can be expressed as

$$E_{\mathbf{b}_C}=\left\{\mathbf{b}_C\,|\left(\mathbf{b}_C-\mathbf{b}_C^c\right)^T\boldsymbol{\Omega}\left(\mathbf{b}_C-\mathbf{b}_C^c\right)\le\varpi^2,\mathbf{b}_C\in\mathbb{R}^P\right\} \tag{25}$$

where $\mathbf{b}_C^c$ is the center of the ellipsoid model; P is the dimension of convex parameters; $\boldsymbol{\Omega}$ is the characteristic matrix which is symmetric and positive; and ϖ is a specific parameter. The shape and direction of the ellipsoid are determined by $\boldsymbol{\Omega}$, and its size is influenced by both $\boldsymbol{\Omega}$ and ϖ. To characterize the ellipsoid model more conveniently, some basic variables are defined firstly. Initially, the center, radius and variance of the convex parameters can be defined by the interval $\mathbf{b}_{Co}^I=\left[\underline{\mathbf{b}}_{Co},\overline{\mathbf{b}}_{Co}\right]$ (o=1, 2,⋯, P)

$$\mathbf{b}_{Co}^c=\frac{\underline{\mathbf{b}}_{Co}+\overline{\mathbf{b}}_{Co}}{2}\quad,\quad\mathbf{b}_{Co}^r=\frac{\overline{\mathbf{b}}_{Co}-\underline{\mathbf{b}}_{Co}}{2}\quad,\quad D\left(\mathbf{b}_{Co}\right)=\left(\mathbf{b}_{Co}^r\right)^2 \tag{26}$$

And the covariance matrix $\mathbf{W}$ can be calculated by

$$\mathbf{W}=\begin{bmatrix}Cov\left(\mathbf{b}_{C1},\mathbf{b}_{C1}\right) & Cov\left(\mathbf{b}_{C1},\mathbf{b}_{C2}\right) & \cdots & Cov\left(\mathbf{b}_{C1},\mathbf{b}_{CP}\right)\\ & Cov\left(\mathbf{b}_{C2},\mathbf{b}_{C2}\right) & \cdots & Cov\left(\mathbf{b}_{C2},\mathbf{b}_{CP}\right)\\ & & \ddots & \vdots\\ Sym & & & Cov\left(\mathbf{b}_{CP},\mathbf{b}_{CP}\right)\end{bmatrix} \tag{27}$$

where $Cov(\mathbf{b}_{Co},\mathbf{b}_{Cl})=\rho(\mathbf{b}_{Co},\mathbf{b}_{Cl})\sqrt{D(\mathbf{b}_{Co})}\sqrt{D(\mathbf{b}_{Cl})}$ is the covariance and $\rho(\mathbf{b}_{Co},\mathbf{b}_{Cl})$ is their correlation coefficient. In fact, the pseudo-inverse matrix of $\mathbf{W}$ is the characteristic matrix $\mathbf{\Omega}$. It may be ill-posed sometimes due to the different magnitude between convex parameters. Thus, convex parameters should be transformed to a dimensionless space by

$$\tilde{\mathbf{b}}_{Co}=\frac{\mathbf{b}_{Co}-\mathbf{b}_{Co}^{c}}{\mathbf{b}_{Co}^{r}} \quad , \quad o=1,2,\cdots,P \tag{28}$$

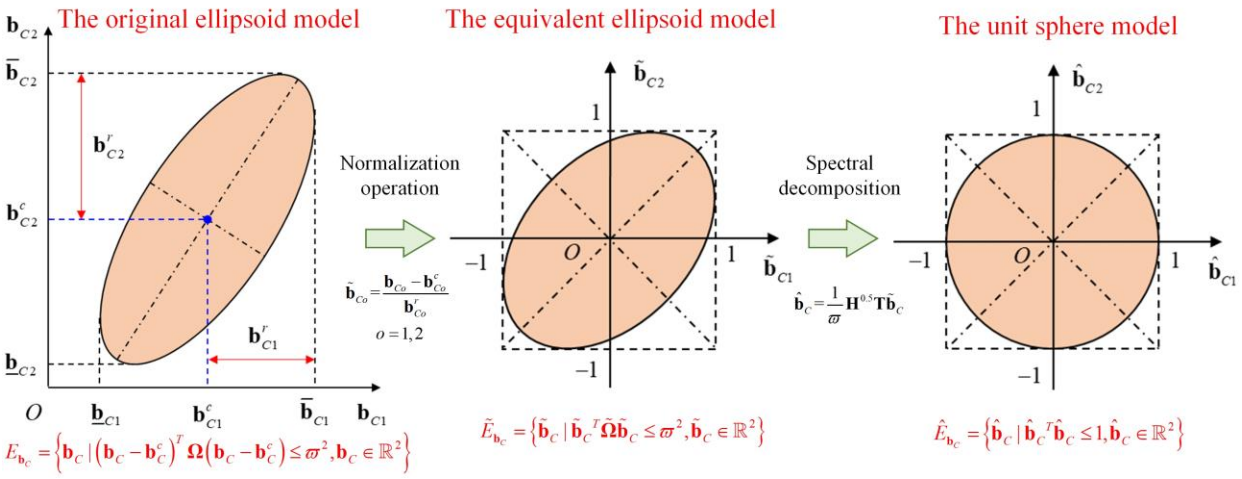

Fig. 3 The convex parameters under different spaces

Then an equivalent ellipsoid model $\tilde{E}_{\mathbf{b}_C}$ can be yielded, i.e.,

$$\tilde{E}_{\mathbf{b}_C}=\left\{\tilde{\mathbf{b}}_C \mid \tilde{\mathbf{b}}_C{}^T\tilde{\mathbf{\Omega}}\tilde{\mathbf{b}}_C\le\varpi^2,\tilde{\mathbf{b}}_C\in\mathbb{R}^P\right\} \tag{29}$$

where $\tilde{\mathbf{\Omega}}$=diag$\left(\mathbf{b}_{Co}^{c}\right)\mathbf{\Omega}$diag$\left(\mathbf{b}_{Co}^{c}\right)$ is the characteristic matrix and diag$\left(\mathbf{b}_{Co}^{c}\right)$ is a diagonal matrix. Taking the spectral decomposition $\tilde{\mathbf{\Omega}}=\mathbf{T}^T\mathbf{H}\mathbf{T}$, a normalized vector can be defined as

$$\hat{\mathbf{b}}_C=\frac{1}{\varpi}\mathbf{H}^{0.5}\mathbf{T}\tilde{\mathbf{b}}_C \tag{30}$$

in which $\mathbf{T}$ is an orthogonal matrix and satisfies $\mathbf{T}^T\mathbf{T}=\mathbf{I}$. $\mathbf{H}$ denotes the diagonal matrix composed of eigenvalues. The convex parameters can be further transformed to a normalized space from the dimensionless space, and a unit hypersphere model can be obtained as

$$\hat{E}_{\mathbf{b}_C}=\left\{\hat{\mathbf{b}}_C \mid \hat{\mathbf{b}}_C{}^T\hat{\mathbf{b}}_C\le 1,\hat{\mathbf{b}}_C\in\mathbb{R}^P\right\} \tag{31}$$

where $\hat{\mathbf{b}}_C$ is the normalized vector regarding the convex parameter $\mathbf{b}_C$. As shown in Fig. 3, the two-dimensional convex parameters are finally encompassed by a circle through twice transformation. Utilizing spherical coordinates $(R,\theta_1,\theta_2,\cdots,\theta_{P-1})$, $R\in[0,1]$, $\theta_{P-1}\in[0,2\pi]$, $\theta_a\in[0,\pi]$ $(a=1,2,\cdots,P-2)$ to signify the unit hypersphere model, we have

$$\begin{cases} \hat{\mathbf{b}}_C = \begin{cases} R\cos\theta_1 \\ R\sin\theta_1\cos\theta_2 \\ R\sin\theta_1\sin\theta_2\cos\theta_3 \\ \vdots \\ R\sin\theta_1\sin\theta_2\ldots\sin\theta_{P-2}\cos\theta_{P-1} \end{cases} \\ \mathbf{b}_C = \varpi\mathbf{T}^T\mathbf{H}^{-0.5}\hat{\mathbf{b}}_C + \mathbf{b}_C^c \end{cases} \tag{32}$$

Since the spherical coordinates are all interval variables, the convex parameters $\mathbf{b}_C$ can be modeled by the interval model eventually.

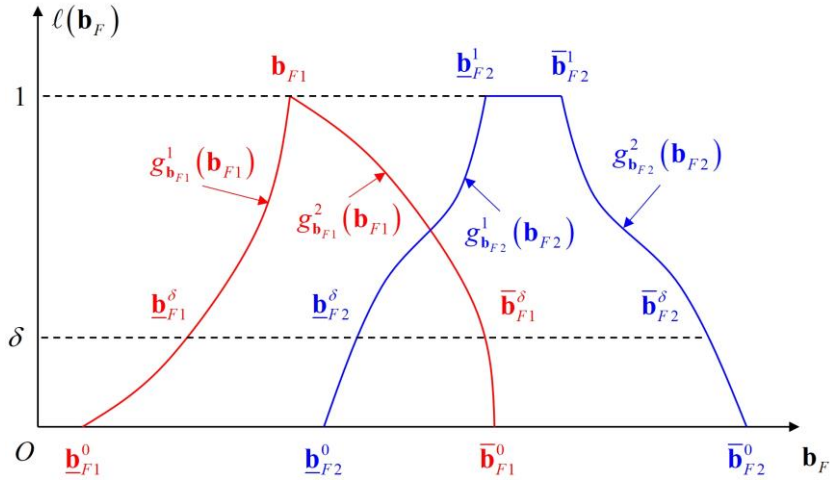

Fig. 4 The description of fuzzy parameters

When it comes to the fuzzy theory in uncertainty analysis, the level-cut strategy is applicable to deal with fuzzy information. The fuzzy parameters $\mathbf{b}_F = \{\mathbf{b}_{F1}, \mathbf{b}_{F2}, \cdots \mathbf{b}_{FQ}\}$ can be generally described by the membership function $\ell(\mathbf{b}_{Fe})$ (e=1, 2, $\cdots$, Q). As debated in Ref. [32], it contains Gaussian type, trapezoid type, triangle type, etc. The membership function $\ell(\mathbf{b}_{Fe})$ is commonly depicted as

$$\ell(\mathbf{b}_{Fe}) = \begin{cases} g^1_{\mathbf{b}_{Fe}}(\mathbf{b}_{Fe}) & \delta^1_{\mathbf{b}_{Fe}} \le \mathbf{b}_{Fe} < \delta^2_{\mathbf{b}_{Fe}} \\ 1 & \delta^2_{\mathbf{b}_{Fe}} \le \mathbf{b}_{Fe} \le \delta^3_{\mathbf{b}_{Fe}} \\ g^2_{\mathbf{b}_{Fe}}(\mathbf{b}_{Fe}) & \delta^3_{\mathbf{b}_{Fe}} < \mathbf{b}_{Fe} \le \delta^4_{\mathbf{b}_{Fe}} \\ 0 & \text{others} \end{cases} \tag{33}$$

where $g^1_{\mathbf{b}_{Fe}}(\mathbf{b}_{Fe})$ and $g^2_{\mathbf{b}_{Fe}}(\mathbf{b}_{Fe})$ embody the monotonically increasing and monotonically decreasing functions related to the fuzzy parameter $\mathbf{b}_{Fe}$, respectively. Given the membership value δ ($\delta \in [0,1]$), the δ-cut fuzzy parameter $\mathbf{b}_{Fe}$ can be expressed as

$$\mathbf{b}^\delta_{Fe} = \{\mathbf{b}_{Fe} | \ell(\mathbf{b}_{Fe}) \ge \delta, \ \ \mathbf{b}_{Fe} \in R\} \tag{34}$$

As shown in Fig. 4, it can be regarded as a truncated interval $\mathbf{b}_{Fe}^{\delta} \in \left[\underline{\mathbf{b}}_{Fe}^{\delta}, \overline{\mathbf{b}}_{Fe}^{\delta}\right]$, whose upper and lower bounds can be given by

$$\begin{aligned} \underline{\mathbf{b}}_{Fe}^{\delta} &= \min\left\{\mathbf{b}_{Fe} | \ell\left(\mathbf{b}_{Fe}\right) \geq \delta, \ \ \mathbf{b}_{Fe} \in R\right\} = \left(g_{\mathbf{b}_{Fe}}^{1}\right)^{-1}(\delta) \\ \overline{\mathbf{b}}_{Fe}^{\delta} &= \max\left\{\mathbf{b}_{Fe} | \ell\left(\mathbf{b}_{Fe}\right) \geq \delta, \ \ \mathbf{b}_{Fe} \in R\right\} = \left(g_{\mathbf{b}_{Fe}}^{2}\right)^{-1}(\delta) \end{aligned} \tag{35}$$

where $\left(g_{\mathbf{b}_{Fe}}^{1}\right)^{-1}(*)$ and $\left(g_{\mathbf{b}_{Fe}}^{2}\right)^{-1}(*)$ are respectively the inverse function of $g_{\mathbf{b}_{Fe}}^{1}\left(\mathbf{b}_{Fe}\right)$ and $g_{\mathbf{b}_{Fe}}^{2}\left(\mathbf{b}_{Fe}\right)$. For this reason, the fuzzy parameters $\mathbf{b}_{F}$ can be investigated by the interval model similarly under any truncated level.

4.2 Uncertain propagation analyses based on Chebyshev-Interval method

If convex uncertainties are only involved, the identified force $\mathbf{f}^{v}(\mathbf{b},t)$ on the v-th FEM node will be an interval term. Then, it will possess fuzzy characters if fuzzy uncertainties are further considered. As described in section 3.1, the interval model is used to characterize the hybrid uncertainties (normalized convex parameters and truncated fuzzy parameters), namely

$$\mathbf{b} \in \mathbf{b}^{I} = \left\{R, \theta_1, \theta_2, \cdots, \theta_{P-1}, \mathbf{b}_{F1}^{\delta}, \mathbf{b}_{F2}^{\delta}, \cdots, \mathbf{b}_{FQ}^{\delta}\right\} \ \Rightarrow \ \mathbf{b} = \left\{\mathbf{b}_1, \mathbf{b}_2, \cdots, \mathbf{b}_{P+Q}\right\} \tag{36}$$

The identified lower/upper boundary can be given by

$$\begin{aligned} \underline{\mathbf{f}}^{v}(\mathbf{b},t) &= \min_{\mathbf{b}\in\mathbf{b}^{I}}\left\{\mathbf{f}(\mathbf{b},t) \,|\, \mathbf{M}(\mathbf{b})\ddot{\mathbf{u}}(\mathbf{b},t) + \mathbf{C}(\mathbf{b})\dot{\mathbf{u}}(\mathbf{b},t) + \mathbf{K}(\mathbf{b})\mathbf{u}(\mathbf{b},t) = \mathbf{f}(\mathbf{b},t)\right\} \\ \overline{\mathbf{f}}^{v}(\mathbf{b},t) &= \max_{\mathbf{b}\in\mathbf{b}^{I}}\left\{\mathbf{f}(\mathbf{b},t) \,|\, \mathbf{M}(\mathbf{b})\ddot{\mathbf{u}}(\mathbf{b},t) + \mathbf{C}(\mathbf{b})\dot{\mathbf{u}}(\mathbf{b},t) + \mathbf{K}(\mathbf{b})\mathbf{u}(\mathbf{b},t) = \mathbf{f}(\mathbf{b},t)\right\} \end{aligned} \tag{37}$$

The Monte Carlo simulation (MCS) and the global optimization algorithm are the most straightforward approaches to calculate the DDL interval with fuzzy bound. However, they are time-consuming and labor-consuming to get global characteristic matrices by repetitive FEM analysis. Besides, some easy but crude methods such as the vertex combination or the Taylor series expansion are developed but they are inaccurate for nonlinear and large uncertainty problems. Herein, an effective uncertainty propagation method based on the Chebyshev orthogonal polynomial (COP) approximation [33] in the multidimensional interval (Chebyshev-Interval) is carried out.

For the sake of simplicity and generality, a one-dimensional interval $b \in b^{I} = \left[\underline{b}, \overline{b}\right]$ is applied to illustrate the details. The COPs are simply defined as

$$\begin{cases} \hbar_0(\tilde{b}) = 1 \ \ , \ \ \hbar_1(\tilde{b}) = \tilde{b} \\ \hbar_{e+1}(\tilde{b}) = 2\tilde{b}\hbar_e(\tilde{b}) - \hbar_{e-1}(\tilde{b}) \end{cases} \quad , \quad \tilde{b} = \frac{2b - (\underline{b} + \overline{b})}{\overline{b} - \underline{b}} \in \left[-1, 1\right] \tag{38}$$

where $\tilde{b}$ is the equivalent mapping of interval parameter b in the standard interval $\left[-1,1\right]$. A

set of linearly independent basis $\prod$=Span$\left\{\hbar_0,\hbar_1,\cdots,\hbar_{\mathfrak{A}}\right\}$ may be generated. In addition, there exists a polynomial $\lambda^*\left(\tilde{b},t\right)\in\prod$ that converges to the continuous function of the uncertain $\mathbf{f}^v(b,t)$ included in the interval $\left[\underline{b},\bar{b}\right]$, namely

$$\int_{\underline{b}}^{\bar{b}}\rho(\tilde{b})\left[\mathbf{f}^v(b,t)-\lambda^*\left(\tilde{b},t\right)\right]^2db=\min_{\lambda\left(\tilde{b},t\right)\in\prod}\int_{\underline{b}}^{\bar{b}}\rho(\tilde{b})\left[\mathbf{f}^v(b,t)-\lambda\left(\tilde{b},t\right)\right]^2db \tag{39}$$

where $\rho(\tilde{b})=\dfrac{1}{\sqrt{1-\tilde{b}^2}}$ is the weight function, $\lambda^*\left(\tilde{b},t\right)=\mu_0^*\hbar_0(\tilde{b})+\mu_1^*\hbar_1(\tilde{b})+\cdots+\mu_{\mathfrak{A}}^*\hbar_{\mathfrak{A}}(\tilde{b})$ $=\sum_{i=0}^{\mathfrak{A}}\mu_i^*\hbar_i(\tilde{b})$ is the best square approximation polynomial. The coefficients $\left\{\mu_0^*,\mu_1^*,\cdots,\mu_{\mathfrak{A}}^*\right\}$ can be got by minimizing the function $\aleph\left(\mu_0,\mu_1,\cdots,\mu_{\mathfrak{A}}\right)=\int_{\underline{b}}^{\bar{b}}\rho(\tilde{b})\left[\mathbf{f}^v(b,t)-\sum_{i=0}^{\mathfrak{A}}\mu_i\hbar_i(\tilde{b})\right]^2db$, whose necessary condition can be given as

$$\frac{\partial\aleph(b)}{\partial\mu_j}=2\int_{\underline{b}}^{\bar{b}}\rho(\tilde{b})\left[\mathbf{f}^v(b,t)-\sum_{i=0}^{\mathfrak{A}}\mu_i\hbar_i(\tilde{b})\right]\left[-\hbar_j(\tilde{b})\right]db=0\quad,\quad j=0,1,\cdots,\mathfrak{A} \tag{40}$$

Based on the orthogonality condition and Gaussian-Chebyshev integration formula, it arrives

$$\mu_j^*=\frac{2}{\pi}\int_{\underline{b}}^{\bar{b}}\frac{\mathbf{f}^v(b,t)\hbar_j(\tilde{b})}{\sqrt{1-\tilde{b}^2}}db\approx\frac{2}{\mathfrak{M}}\sum_{e=1}^{\mathfrak{M}}\mathbf{f}^v(b^e,t)\hbar_j(\tilde{b}^e) \tag{41}$$

where $\tilde{b}^1,\tilde{b}^2,\cdots,\tilde{b}^{\mathfrak{M}}$ are the Gaussian interpolation points (GIPs), which can be determined by the zero-points of a $\mathfrak{M}$-order COP. The homologous points $b^1,b^2,\cdots,b^{\mathfrak{M}}$ in the original interval can be given by

$$\tilde{b}^e=\cos\left(\frac{2e-1}{2\mathfrak{M}}\pi\right)\quad,\quad b^e=\frac{(\underline{b}+\bar{b})+\tilde{b}^e(\bar{b}-\underline{b})}{2}\quad,\quad e=1,2,\cdots,\mathfrak{M} \tag{42}$$

In general, $\mathfrak{M}\geq\mathfrak{A}$+1 should be fulfilled to minimize the integration error [34].

Below, apply the one-dimensional uncertainty $b\in b^I$ to the multi-dimensional cases $\mathbf{b}\in\mathbf{b}^I$. Obviously, the nonlinear degree for the angle interval $\theta_{P-1}\in[0,2\pi]$ and $\theta_a\in[0,\pi]$ of convex parameters is higher than that for the δ-cut interval of fuzzy parameters. Thus, to reduce unnecessary calculation but ensure precision, the multidimensional COP with different orders is used to surrogate the function $\mathbf{f}^v(\mathbf{b},t)$. The multi-dimensional best square approximation polynomial over the convex-fuzzy hybrid interval can be written as

$$\lambda^*\left(\tilde{\mathbf{b}},t\right)=\sum_{i_1=0}^{\mathfrak{A}_1}\sum_{i_2=0}^{\mathfrak{A}_2}\cdots\sum_{i_{P+Q}=0}^{\mathfrak{A}_{P+Q}}\left(\frac{1}{2}\right)^{\mathbb{S}}\mu_{i_1i_2\cdots i_{P+Q}}^*\hbar_{i_1i_2\cdots i_{P+Q}}(\tilde{\mathbf{b}}_1,\tilde{\mathbf{b}}_2,\cdots,\tilde{\mathbf{b}}_{P+Q}) \tag{43}$$

where $\mathbb{S}$ is the total number of *zero*(s) occurring in the subscript $i_1i_2\cdots i_{P+Q}$; $\mathfrak{A}_1,\mathfrak{A}_2,\cdots\mathfrak{A}_{P+Q}$ are the orders of each-dimensional COP; $\mu_{i_1i_2\cdots i_{P+Q}}^*$ is the undetermined COP coefficient; $\hbar_{i_1i_2\cdots i_{P+Q}}(\tilde{\mathbf{b}}_1,\tilde{\mathbf{b}}_2,\cdots,\tilde{\mathbf{b}}_{P+Q})$ is the $P+Q$-dimensional COP. The multidimensional COP can be

defined as the tensor product of each one-dimensional COP, namely

$$\begin{aligned}\hbar_{i_1 i_2 \cdots i_{P+Q}}(\mathbf{b}) &= \hbar_{i_1 i_2 \cdots i_{P+Q}}(\tilde{\mathbf{b}}_1, \tilde{\mathbf{b}}_2, \cdots, \tilde{\mathbf{b}}_{P+Q}) = \prod_{\iota=1}^{P+Q} \hbar_{i_\iota}(\tilde{\mathbf{b}}_\iota) \quad , \quad i_\iota = 0,1,2,\cdots \mathfrak{A}_\iota \\ \tilde{\mathbf{b}}_\iota &= \frac{2\mathbf{b}_\iota - (\underline{\mathbf{b}}_\iota + \overline{\mathbf{b}}_\iota)}{\overline{\mathbf{b}}_\iota - \underline{\mathbf{b}}_\iota} \in [-1,1] \quad , \quad \iota = 1,2,\cdots,P+Q\end{aligned} \tag{44}$$

As stated by Eq. (41) for a one-dimensional issue, the coefficient $\mu^*_{i_1 i_2 \cdots i_{P+Q}}$ is detailed as

$$\begin{aligned}\mu^*_{i_1 i_2 \cdots i_{P+Q}} &= \left(\frac{2}{\pi}\right)^{P+Q} \int_{\underline{\mathbf{b}}_1}^{\overline{\mathbf{b}}_1} \int_{\underline{\mathbf{b}}_2}^{\overline{\mathbf{b}}_2} \cdots \int_{\underline{\mathbf{b}}_{P+Q}}^{\overline{\mathbf{b}}_{P+Q}} \frac{\mathbf{f}^v(\mathbf{b},t)\hbar_{i_1 i_2 \cdots i_{P+Q}}(\mathbf{b})}{\sqrt{1-\tilde{\mathbf{b}}_1^{\,2}}\sqrt{1-\tilde{\mathbf{b}}_2^{\,2}}\cdots\sqrt{1-\tilde{\mathbf{b}}_{P+Q}^{\,2}}} d\tilde{\mathbf{b}}_1 d\tilde{\mathbf{b}}_2 \cdots d\tilde{\mathbf{b}}_{P+Q} \\ &= \prod_{\iota=1}^{P+Q}\left(\frac{2}{\mathfrak{M}_\iota}\right) \sum_{e_1=1}^{\mathfrak{M}_1} \sum_{e_2=1}^{\mathfrak{M}_2} \cdots \sum_{e_{P+Q}=1}^{\mathfrak{M}_{P+Q}} \left[\mathbf{f}^v(\mathbf{b}_1^{e_1}, \mathbf{b}_2^{e_2}, \cdots, \mathbf{b}_{P+Q}^{e_{P+Q}}, t) \prod_{\iota=1}^{P+Q} \hbar_{i_\iota}(\tilde{\mathbf{b}}_\iota^{e_\iota}) \right]\end{aligned} \tag{45}$$

where $\mathfrak{M}_1, \mathfrak{M}_2, \cdots, \mathfrak{M}_{P+Q}$ denote the each-dimensional number of GIPs. $\tilde{\mathbf{b}}_\iota^{e_1}, \tilde{\mathbf{b}}_\iota^{e_2}, \cdots, \tilde{\mathbf{b}}_\iota^{\mathfrak{M}_\iota}$ and $\mathbf{b}_\iota^{e_1}, \mathbf{b}_\iota^{e_2}, \cdots, \mathbf{b}_\iota^{\mathfrak{M}_\iota}$ are GIPs and corresponding original parameters in the ι-th dimension, i.e.,

$$\tilde{\mathbf{b}}_\iota^{e_\iota} = \cos\left(\frac{2e_\iota - 1}{2\mathfrak{M}_\iota}\pi\right) \quad , \quad \mathbf{b}_\iota^{e_\iota} = \frac{(\underline{\mathbf{b}}_\iota + \overline{\mathbf{b}}_\iota) + \tilde{\mathbf{b}}_\iota^{e_\iota}(\overline{\mathbf{b}}_\iota - \underline{\mathbf{b}}_\iota)}{2} \quad , \quad e_\iota = 1,2,\cdots,\mathfrak{M}_\iota \tag{46}$$

Additionally, the configuration schemes of GIPs are plotted in Fig. 5 for two low-dimensional issues. Similarly, $\mathfrak{M}_\iota \geq \mathfrak{A}_\iota + 1$ should be guaranteed to minimize the integration error.

Once the series of COP coefficients are determined, the properties of force $\mathbf{f}^v(\mathbf{b},t)$ in the convex-fuzzy uncertain domain can be expressed by an explicit multivariate function. Then, Eq. (37) can be replaced by finding the maximum and minimum of the COP function $\lambda^*(\tilde{\mathbf{b}},t)$, which is easy to implement without calling too much FEM calculation. That is

$$\underline{\mathbf{f}}^v(\mathbf{b},t) = \min_{\mathbf{b}\in\mathbf{b}^I}\left\{\lambda^*(\tilde{\mathbf{b}},t)\right\} \quad , \quad \overline{\mathbf{f}}^v(\mathbf{b},t) = \max_{\mathbf{b}\in\mathbf{b}^I}\left\{\lambda^*(\tilde{\mathbf{b}},t)\right\} \tag{47}$$

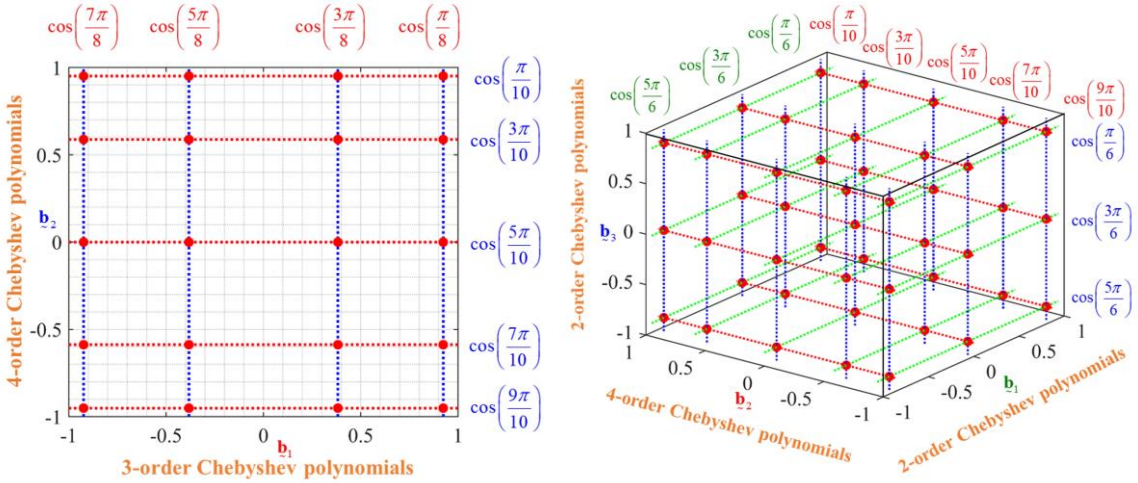

(a) Two-dimensional issue (b) Three-dimensional issue

Fig. 5 The configuration scheme of GIPs

5 Implementation of the load identification procedure

To clearly manifest the overall process of the given uncertain temporal and spatial load identification strategy, the operation logic is displayed in Fig. 6, mainly including dynamic inverse, RBF approximation and uncertainty treatment. Moreover, the pseudo-code of DDL identification with the deterministic parameter $\mathbf{b}'$ and hybrid uncertainty analysis with the Chebyshev-Interval method at δ-cut fuzzy parameters are provided in **Algorithm 1** and **Algorithm 2**. Specific procedures are successively summarized as below.

Step 1. Preset the conditions, including the global characteristic matrices ($\mathbf{M}(\mathbf{b})$, $\mathbf{C}(\mathbf{b})$ and $\mathbf{K}(\mathbf{b})$) of the FEM model, the sequence of acceleration signals, control parameters β and γ, the time increment Δt, the coordinates $\mathbf{L}$ of FEM nodes, the coefficients τ and λ in hierarchical clustering, the ellipsoid model of convex parameters $\mathbf{b}_C$ and the membership function of fuzzy parameters $\mathbf{b}_F$.

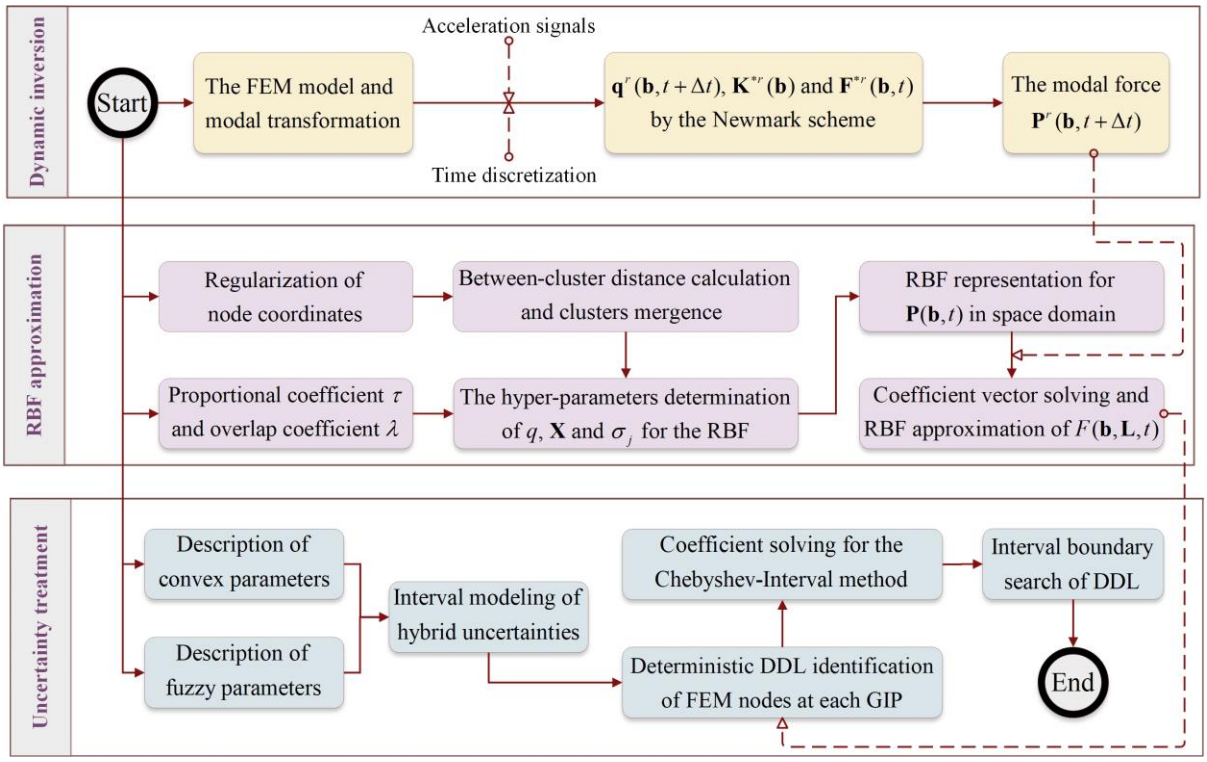

Fig. 6 The procedure of temporal and spatial load identification under hybrid uncertainties

Step 2. Transform the ellipsoid model $E_{\mathbf{b}_C}$ to the unit hypersphere model $\hat{E}_{\mathbf{b}_C}$, obtain the δ-cut interval $\mathbf{b}_{Fe}^{\delta}$ of fuzzy parameters, and perform the interval modeling for hybrid uncertainties $\mathbf{b} \in \mathbf{b}^I$. Determine the GIPs $\tilde{\mathbf{b}}_t^{e_1}, \tilde{\mathbf{b}}_t^{e_2}, \cdots, \tilde{\mathbf{b}}_t^{\mathfrak{M}_t}$ $(t = 1, 2, \cdots, P+Q)$.

Step 3. Calculate modal responses $\mathbf{q}^r(\mathbf{b},t)$, $\dot{\mathbf{q}}^r(\mathbf{b},t)$, $\ddot{\mathbf{q}}^r(\mathbf{b},t)$ and $\mathbf{q}^r(\mathbf{b},t+\Delta t)$ based on the Newmark iteration and modal transformation strategies. Inverse the modal load $\mathbf{P}^r(\mathbf{b},t+\Delta t)$ via Eqs. (5), (6) and (19).

Step 4. Based on the hierarchical-clustering method, determine the number q of RBF centers, the center set $\mathbf{X}$ and the variance σ_j for the RBF interpolation.

Step 5. Calculate the RBF coefficients through Eqs. (22)-(24) and express the DDL on each FEM node. Judge whether the DDLs of all GIPs have been identified. If not, continue to perform Step 3 and Step 4; otherwise, proceed to the next step.

Step 6. Calculate the COP coefficients through Eqs. (45)-(46) and construct the Chebyshev-Interval method based on the best square approximation. Finding its maximum and minimum as the upper and lower bound.

Algorithm 1 DDL identification with the deterministic parameter $\mathbf{b}'$

Input: The characteristic matrices $\mathbf{M}(\mathbf{b}')$, $\mathbf{C}(\mathbf{b}')$ and $\mathbf{K}(\mathbf{b}')$, the control parameters β and γ, the time increment Δt, the acceleration signals, the FEM coordinates, and the coefficients τ and λ

Output: The DDL of each FEM node in the time history

1: Calculate the modal acceleration: $\ddot{\mathbf{q}}(\mathbf{b}',t) \leftarrow \left[\mathbf{\Phi}_k(\mathbf{b}')\right]^{+} \ddot{\mathbf{u}}(t)$

2: **While** $0 \le t \le T - \Delta t$, **Do**

3: Inverse the modal force $\mathbf{P}^r(\mathbf{b}',t+\Delta t) \leftarrow \mathbf{K}^{*r}(\mathbf{b}')\mathbf{q}^r(\mathbf{b}',t+\Delta t) - \mathbf{F}^{*r}(\mathbf{b}',t)$

4: $t = t + \Delta t$

5: **End While**

6: Regularize the coordinate of the FEM node: $\tilde{\mathbf{L}}^i = \left[2\mathbf{L}^i - \left(A_{\max} + A_{\min}\right)\right] / \left(A_{\max} - A_{\min}\right)$, $i = 1,\cdots,\kappa$

7: Regard $\tilde{\mathbf{L}}^i$ ($i = 1,\cdots,\kappa$) as the initial clusters and calculate the Euclidean distance: $\xi_{vw} \leftarrow \left\|\tilde{\mathbf{L}}_v^i - \tilde{\mathbf{L}}_w^i\right\|$

8: **While** the number of clusters is more than 1, **Do**

9: Merge the two clusters with the nearest distance, then calculate between-cluster distances

$$\zeta_{po} \leftarrow \frac{1}{\Delta_p \Delta_o} \sum_{\tilde{\mathbf{L}}_v \in \tilde{\mathrm{E}}_p} \sum_{\tilde{\mathbf{L}}_w \in \tilde{\mathrm{E}}_o} \xi_{vw}$$

10: **End While**

11. Determine the hyper-parameters of RBF based on hierarchical clustering:

$$q \leftarrow m - \varepsilon \ \left(\zeta^{(\varepsilon)} \ge \tau \zeta^{m-1}\right),\ \mathbf{x}_j \leftarrow \frac{1}{\Delta_j} \sum_{\tilde{\mathbf{L}}_* \in \tilde{\mathrm{E}}_j} \tilde{\mathbf{L}}_*\ ,\ \sigma_j \leftarrow \lambda \Im_j \ \left(\Im_j \leftarrow \min\left(\left\|\mathbf{x}_j - \mathbf{x}_i\right\|\right)\right)$$

12: Generate the RBF space, then calculate the RBF coefficient:

$$\boldsymbol{\chi}(\mathbf{b},t) = \left\{ \begin{bmatrix} \mathbf{\Phi}_k^T(\mathbf{b}')\mathbf{T}_f \mathbf{\Psi}(\tilde{\mathbf{L}}) \\ \mathbf{\Gamma}(\mathbf{X}) \end{bmatrix}^T \begin{bmatrix} \mathbf{\Phi}_k^T(\mathbf{b}')\mathbf{T}_f \mathbf{\Psi}(\tilde{\mathbf{L}}) \\ \mathbf{\Gamma}(\mathbf{X}) \end{bmatrix} \right\}^{-1} \begin{bmatrix} \mathbf{\Phi}_k^T(\mathbf{b}')\mathbf{T}_f \mathbf{\Psi}(\tilde{\mathbf{L}}) \\ \mathbf{\Gamma}(\mathbf{X}) \end{bmatrix}^T \begin{bmatrix} \mathbf{P}(\mathbf{b}',t) \\ \mathbf{0} \end{bmatrix}$$

13: Approximate the DDL of the v-th FEM node: $\mathbf{f}^v(\mathbf{b},t) \leftarrow \mathbf{\Xi}(\tilde{\mathbf{L}}_v)\boldsymbol{\chi}(\mathbf{b},t)$

6 Validation of the proposed method with examples

In order to clarify the feasibility of the developed methodology, 3 numerical examples

will be investigated in this section. Moreover, the MATLAB codes, model datasets, acceleration signals and identified results are provided on the webpage (https://bhpan.buaa.edu.cn:443/link/D9810C398CA9CA8B0D9963770F8E9B10) to shed light on the procedure and validation. In the first example, a cantilever beam structure imposed by one-dimensional DDLs is discussed to mainly illustrate the superiority of the proposed uncertain propagation method. Then, an equivalent rudder structure subjected to two-dimensional DDLs is involved to clarify the feasibility of the hierarchical-clustering-based RBF approximation. Eventually, a more complicated three-dimensional wing structure is further analyzed to explore the effects of sensor deployment and RBF parameters.

Algorithm 2 Hybrid uncertainty analysis with the Chebyshev-Interval method at δ -cut fuzzy parameters

Input: The ellipsoid model of convex parameters $\mathbf{b}_C$ and the membership function of fuzzy parameters $\mathbf{b}_F$

Output: The load interval of each FEM node at time t

1: Transform the ellipsoid model $E_{\mathbf{b}_C}$ to an equivalent model $\tilde{E}_{\mathbf{b}_C}$, then to a unit hypersphere model $\hat{E}_{\mathbf{b}_C}$

2: Represent the convex parameters by spherical coordinates $\left(R,\theta_1,\theta_2,\cdots,\theta_{P-1}\right)$

3: Obtain the interval $\mathbf{b}_{Fe}^{\delta}\in\left[\underline{\mathbf{b}}_{Fe}^{\delta},\overline{\mathbf{b}}_{Fe}^{\delta}\right]$ at the δ -cut level of the fuzzy variable $\mathbf{b}_{Fe}$

4: Construct the interval model of hybrid uncertainties: $\mathbf{b}\leftarrow\left\{R,\theta_1,\theta_2,\cdots,\theta_{P-1},\mathbf{b}_{F1}^{\delta},\mathbf{b}_{F2}^{\delta},\cdots,\mathbf{b}_{FQ}^{\delta}\right\}$

5: Determine the order $\mathfrak{A}_1,\mathfrak{A}_2,\cdots\mathfrak{A}_{P+Q}$ and GIPs for each-dimensional COP:

$\tilde{\mathbf{b}}_{\iota}^{e_\iota}\leftarrow\cos\left[(2e_\iota-1)\pi/2\mathfrak{M}_\iota\right]$, $e_\iota\leftarrow1,2,\cdots,\mathfrak{M}_\iota$, $\iota\leftarrow1,2,\cdots,P+Q$

6: Identify the DDL $\mathbf{f}^{\nu}(\mathbf{b}_1^{e_1},\mathbf{b}_2^{e_2},\cdots,\mathbf{b}_{P+Q}^{e_{P+Q}},t)$ on each GIP based on **Algorithm 1**

7: Calculate the COP coefficient: $\mu_{i_1i_2\cdots i_{P+Q}}^{*}\leftarrow\prod_{\iota=1}^{P+Q}\left(\frac{2}{\mathfrak{M}_\iota}\right)\sum_{e_1=1}^{\mathfrak{M}_1}\sum_{e_2=1}^{\mathfrak{M}_2}\cdots\sum_{e_{P+Q}=1}^{\mathfrak{M}_{P+Q}}\left[\mathbf{f}^{\nu}(\mathbf{b}_1^{e_1},\mathbf{b}_2^{e_2},\cdots,\mathbf{b}_{P+Q}^{e_{P+Q}},t)\prod_{\iota=1}^{P+Q}\hbar_{i_\iota}(\tilde{\mathbf{b}}_\iota^{e_\iota})\right]$

8: Build the multi-dimensional best square approximation polynomial:

$$\lambda^{*}\left(\tilde{\mathbf{b}},t\right)\leftarrow\sum_{i_1=0}^{\mathfrak{A}_1}\sum_{i_2=0}^{\mathfrak{A}_2}\cdots\sum_{i_{P+Q}=0}^{\mathfrak{A}_{P+Q}}\left(\frac{1}{2}\right)^{\mathbb{S}}\mu_{i_1i_2\cdots i_{P+Q}}^{*}\hbar_{i_1i_2\cdots i_{P+Q}}(\tilde{\mathbf{b}}_1,\tilde{\mathbf{b}}_2,\cdots,\tilde{\mathbf{b}}_{P+Q})$$

9: Find the extreme as the load boundary: $\underline{\mathbf{f}}^{\nu}(\mathbf{b},t)\leftarrow\min_{\mathbf{b}\in\mathbf{b}^I}\left\{\lambda^{*}\left(\tilde{\mathbf{b}},t\right)\right\}$, $\overline{\mathbf{f}}^{\nu}(\mathbf{b},t)\leftarrow\max_{\mathbf{b}\in\mathbf{b}^I}\left\{\lambda^{*}\left(\tilde{\mathbf{b}},t\right)\right\}$

Three evaluation indexes for each FEM node are additionally defined to quantitatively evaluate the identified results, including the peak relative error (*PRE*), the normalized mean squared error (*NMSE*) and the relative deviation of peak interval (*RDPI*) in the following

$$PRE^{\nu}=\left|\frac{\mathbf{f}^{\nu}(\mathbf{b}^{*},t_{\max}^{\nu})-F_{real}(\mathbf{L}_{\nu},t_{\max}^{\nu})}{F_{real}(\mathbf{L}_{\nu},t_{\max}^{\nu})}\right|\times100\%\quad,\quad NMSE^{\nu}=\frac{\sum_{i=1}^{S}\left[\mathbf{f}^{\nu}(\mathbf{b}^{*},t_i)-F_{real}(\mathbf{L}_{\nu},t_i)\right]^2}{\sum_{i=1}^{S}F_{real}(\mathbf{L}_{\nu},t_i)^2}$$
$$RDPI^{\nu}=\left|\frac{\overline{\mathbf{f}}^{\nu}(\mathbf{b},t_{\max}^{\nu})-\underline{\mathbf{f}}^{\nu}(\mathbf{b},t_{\max}^{\nu})}{F_{real}(\mathbf{L}_{\nu},t_{\max}^{\nu})}\right|\times100\% \tag{48}$$

where $t_{\max}^{v}$ is the time step with maximum load amplitude for the v-th FEM node; $\mathbf{b}^{*}$ benchmark the nominal parameter composed by the center of convex variables ($\mathbf{b}_{C}^{c}$) and the center value of 1-cut fuzzy variables ($\mathbf{b}_{F}^{1}$); $F_{real}(\mathbf{L}_{v},t_{\max}^{v})$ and $\mathbf{f}^{v}(\mathbf{b}^{*},t_{\max}^{v})$ denote the real /identified loads at time $t_{\max}^{v}$; $F_{real}(\mathbf{L}_{v},t_{i})$ and $\mathbf{f}^{v}(\mathbf{b}^{*},t_{i})$ represent corresponding loads at the i-th sampling instant; and $\overline{\mathbf{f}}^{v}(\mathbf{b},t_{\max}^{v})$ and $\underline{\mathbf{f}}^{v}(\mathbf{b},t_{\max}^{v})$ are the upper/lower bounds at time $t_{\max}^{v}$.

6.1 A cantilever beam structure

As illustrated in Fig. 7, a one-dimensional cantilever beam structure with a length of 1m will host the basis of this example. Through the FEM, it is discretized into 10 elements with 11 nodes. Considering the multi-source uncertainties, the elastic modulus and the density are deemed as fuzzy parameters, whose membership functions are plotted in Fig. 8. The cross-section and the moment of inertia are regarded as convex parameters with the correlation coefficient of 0.5, whose characteristics are listed in Table 1. A lateral DDL $f(x,t)=200(1+x)(1.5-x)\sin(4\pi t)$ is applied in the DOF2 direction, and the time settings are taken as T =2s and Δt =0.001s. The lateral acceleration signals of node 4, node 7 and node 10 simulated by FEM analysis at the nominal parameter are utilized for the uncertainty-oriented DDL identification.

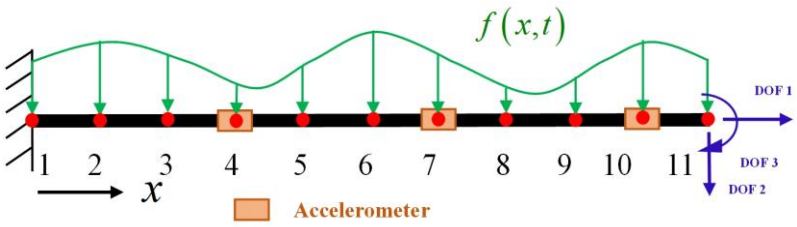

Fig. 7 The one-dimensional cantilever beam structure

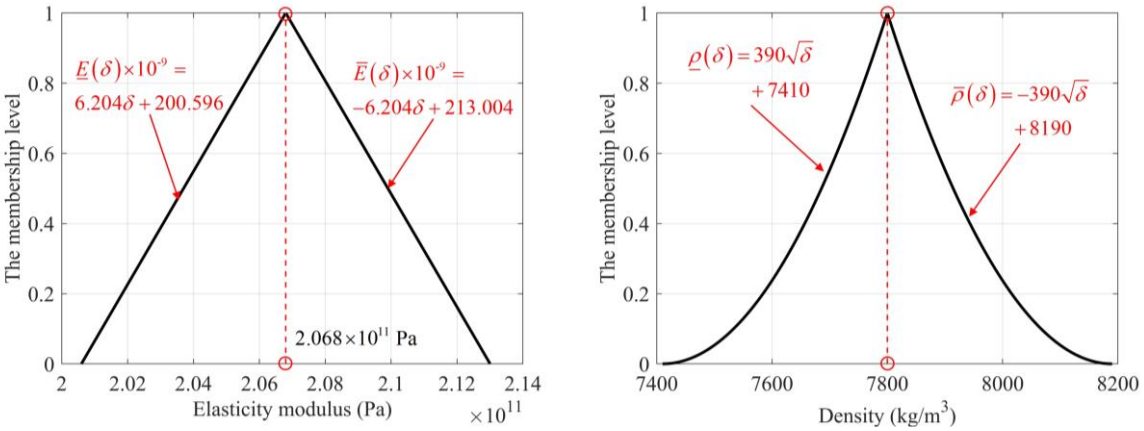

(a) Elasticity modulus (b) Density

Fig. 8 The description of fuzzy parameters

As revealed in Ref. [5], the COPs with 2 orders can completely reflect the changing trend of uncertain loads on the fuzzy uncertain domain at any truncated level. Besides, 2-

order COP can also ensure the uncertainty propagation accuracy for the variable R because the solution of Eq. (37) will appear at the boundary of the ellipsoid domain based on convex optimization theory. To get the suitable order of variable θ in Eq. (43), the COPs with 2, 3, 4, 5 orders are employed respectively to calculate the load intervals at 0-cut fuzzy parameters. The each-dimensional number of GIPs is assigned by $\mathfrak{M}_t = \mathfrak{A}_t + 1$. In addition, the MCS is introduced as the reference solution of uncertainty propagation.

Table 1 The center and radius of convex parameters

Convex parameters	Center	Radius
The cross-section (mm^2)	100	5
The moment of inertia (mm^4)	833.333	25

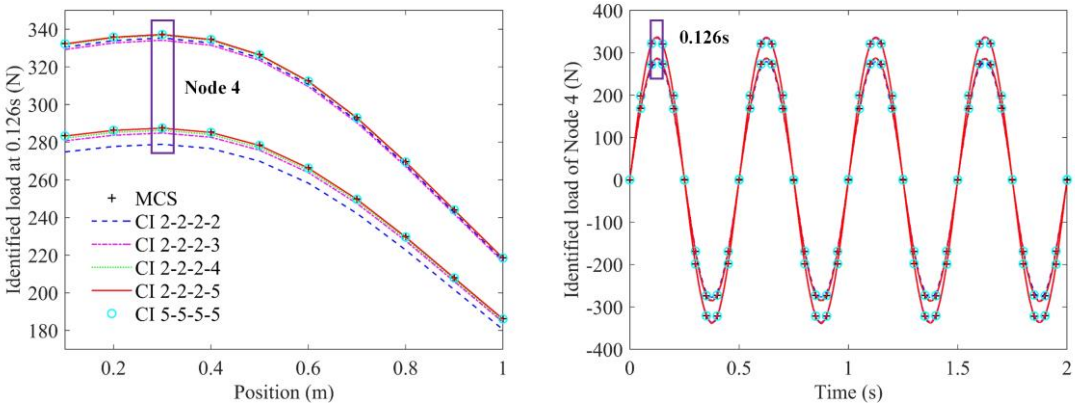

(a) In space domain (b) In time domain

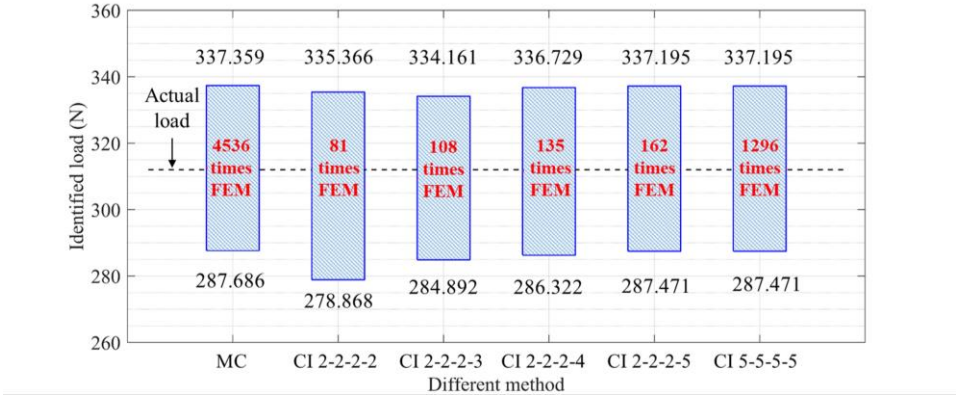

(c) Node 4 at 0.126s

Fig. 9 The DDL intervals at 0-cut fuzzy parameters

The DDL intervals in space domain at 0.126s (maximum load in the time history) and the DDL intervals in time domain of node 4 (maximum load of all FEM nodes) are shown in Fig. 9 (a) and (b), and the specific information of node 4 at 0.126s is observed in Fig. 9 (c), in which 'CI a-b-c-d' means that the orders of COP regarding elastic modulus, density, R and θ are a, b, c and d, respectively in the Chebyshev-Interval method. It indicates that with the order of the variable θ increasing from 2 to 5, the load interval becomes closer to the MSC result. The relative error between CI 2-2-2-5 and MCS is only 0.049% and 0.075% for the

upper and lower bounds without overestimation and underestimation of interval calculation. When the same high-order COPs in each dimension as proposed in Ref. (CI 5-5-5-5) are involved, the load interval is identical compared with CI 2-2-2-5, but the FEM analysis times increase sharply to identify the DDLs at more GIPS. It can be concluded that the accuracy and efficiency of uncertainty propagation can be guaranteed together by the developed Chebyshev-Interval method.

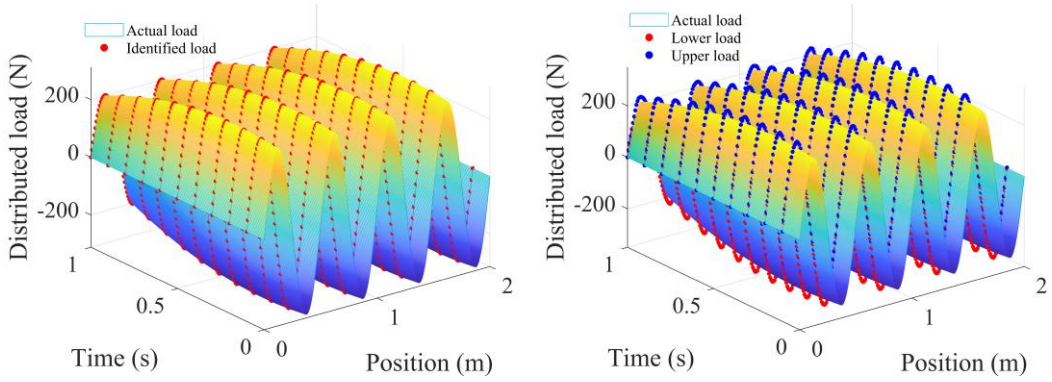

(a) The DDL with nominal parameters (b) The interval at 0-cut fuzzy parameters

Fig. 10 The identified DDL (every 10 steps) for the cantilever beam structure

Table 2 The evaluation results for the cantilever beam structure

Node	**2**	**3**	**4**	**5**	**6**
PRE (%)	0.170	0.400	0.019	0.516	0.692
NMSE (10^{-5})	1.534	2.610	0.041	2.927	5.817
RDPI (%)	15.888	15.861	15.937	16.025	16.061
Node	**7**	**8**	**9**	**10**	**11**
PRE (%)	0.375	0.338	1.044	0.992	1.052
NMSE (10^{-5})	2.341	0.700	8.957	8.252	12.582
RDPI (%)	16.016	15.907	15.815	15.838	16.177

The identified DDLs at the nominal parameter are plotted in Fig. 10 (a), and the load boundaries considering hybrid uncertainties at 0-cut fuzzy parameters are provided in Fig. 10 (b). The evaluation indexes (*PRE*, *NMSE* and *RDPI*) of each FEM node are listed in Table 2. Under different truncated levels (δ =0,.0.2, 0.4, 0.6, 0.8 and 1), the fuzzy interval bounds in space domain at 0.126s and those in time domain of node 4 are demonstrated in Fig. 11. As we can see, the maximum *PRE* is 1.053% and the maximum *NMSE* is 1.177×10^{-3}. Thus, the proposed deterministic DDL identification combining RBF approximation and inverse Newmark iteration can work perfectly for the beam structure. With 0-cut fuzzy parameters, the *RDPI* of each node is around 16%, and the load boundaries can envelop the actual load either in time distribution or spatial distribution.

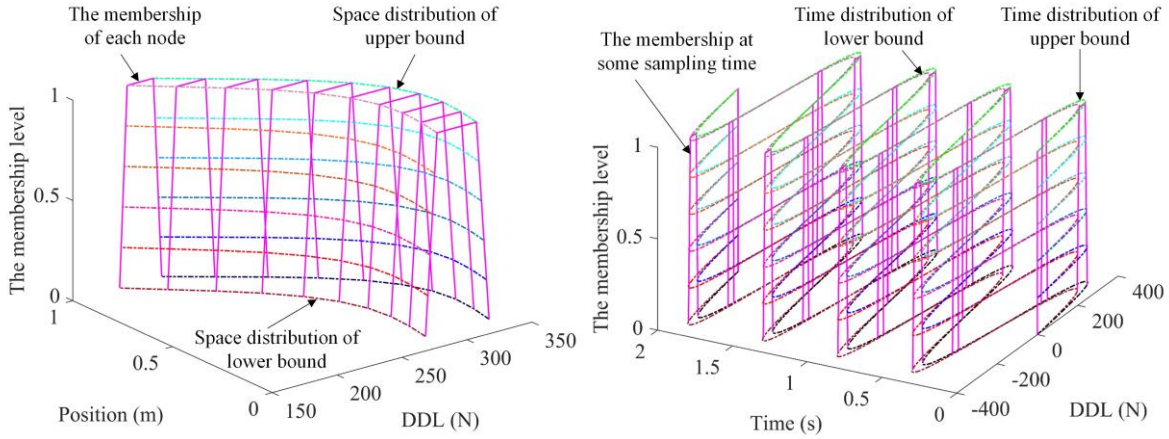

(a) In space domain (b) In time domain (every 100 step)

Fig. 11 The fuzzy interval bounds of DDLs under different membership levels

6.2 An equivalent rudder structure

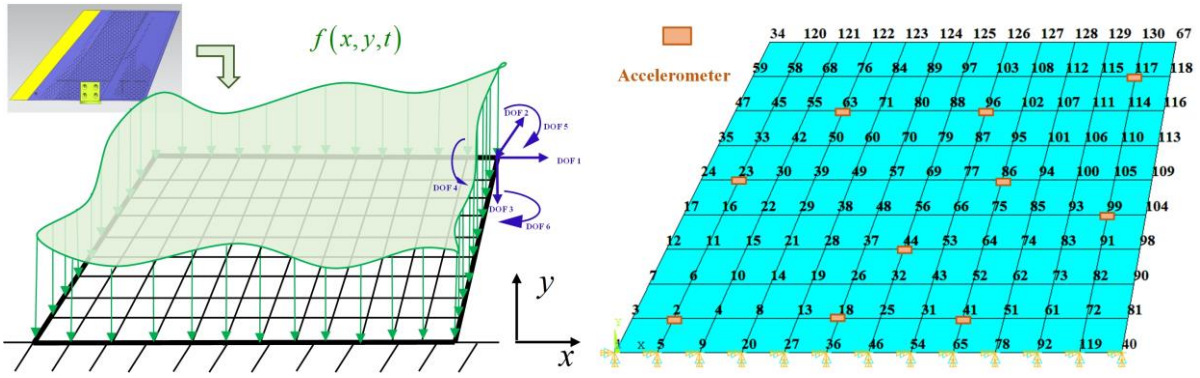

(a) The schematic diagram (b) The FEM model and sensor placement

Fig. 12 The two-dimensional equivalent rudder structure

To affirm the feasibility of the presented methodology for two-dimensional cases, an equivalent rudder structure is further investigated as displayed in Fig. 12. In order to reduce the complexity of FEM analysis, the rudder structure is simplified as an anisotropic plate structure with a thickness of 5mm. The equivalent process has been expounded by our previous works in Ref. [35]. The coordinates are regularized to a standard interval $\tilde{x}, \tilde{y} \in [-1,1]$. The equivalent material properties without uncertainties are listed in Table 3. It is discretized by 9×12 four-node shell elements with 130 nodes and is supported on the root. And it is subjected to a transverse DDL with a duration of 1s and a frequency of 1000 Hz. The layout of accelerometers is plotted in Fig. 12 (b).

Table 3 The material properties for equivalent plate structure

Properties	E_{11} (Pa)	E_{22} (Pa)	E_{33} (Pa)	ν_{12}	ν_{23}
Values	1.9065×10^{11}	1.9123×10^{11}	4.893×10^{10}	0.19	0.25
Properties	ν_{31}	G_{12} (Pa)	G_{23} (Pa)	G_{31} (Pa)	ρ (kg/m^3)
Values	0.069	4.694×10^{10}	1.779×10^{10}	1.46×10^{10}	2380

Table 4 The different expressions of DDLs under 4 cases

Condition	DDL expression
Case 1	$F=\left[-15(\tilde{x}+5)^3+60\tilde{x}^2+750\tilde{x}+150(\tilde{y}+5)^{1.5}+240\tilde{y}+3450\right]\sin(12\pi t)e^{-t}$
Case 2	$F=\left[300\tilde{x}^2+400\tilde{y}^2-250\tilde{x}+480\tilde{y}+975\right]\left[\sin(8\pi t)+\sin(12\pi t)\right]$
Case 3	$F=\left[1000\tilde{x}-500\tilde{y}+2500\right]\sin\left[10\pi(1-t)^{1.5}-10\pi\right]$
Case 4	$F=\left[100\tilde{y}^2+100\lvert\tilde{x}\rvert+200\tilde{y}+150\right]\lvert 2\sin(16\pi t)-3\sin(12\pi t)\rvert$

Table 5 The deterministic identified DDL for the rudder structure using different strategies

Case	In space domain	In time domain
Case 1	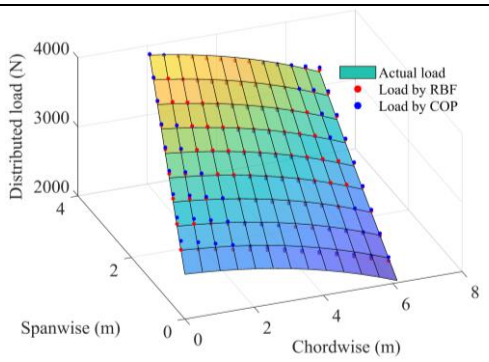	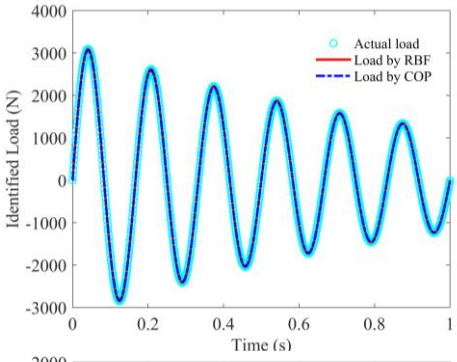
Case 2	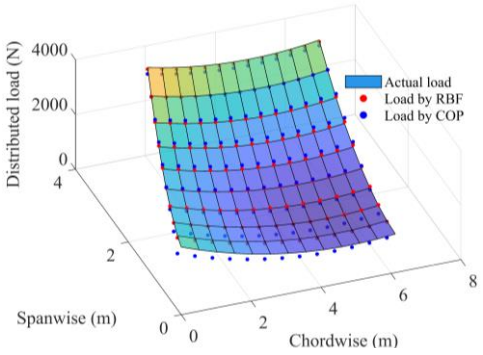	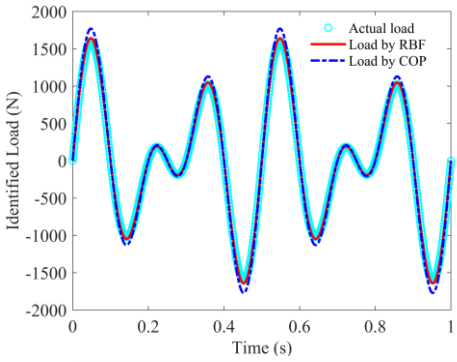
Case 3	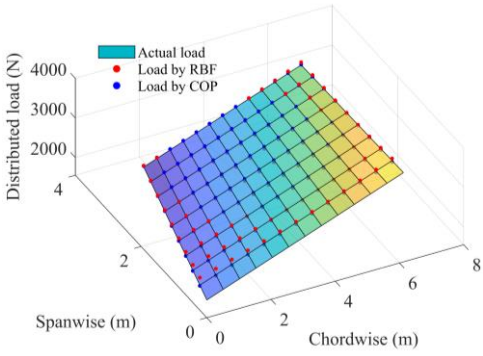	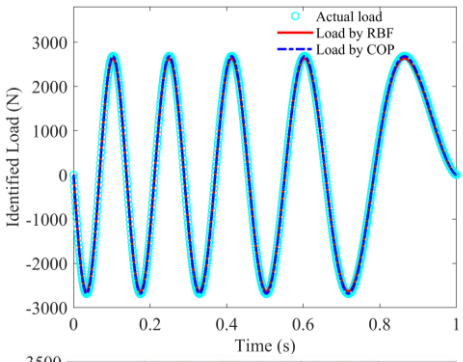
Case 4	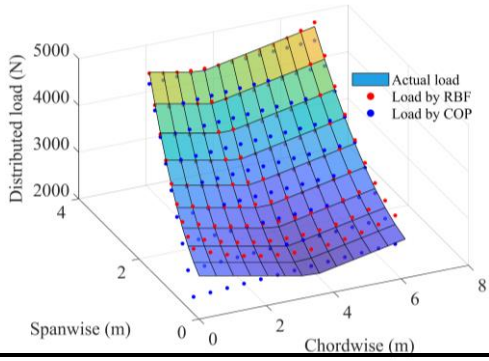	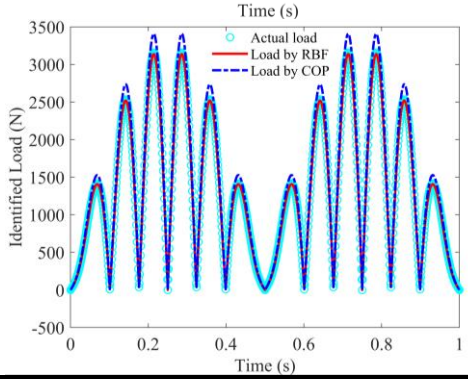

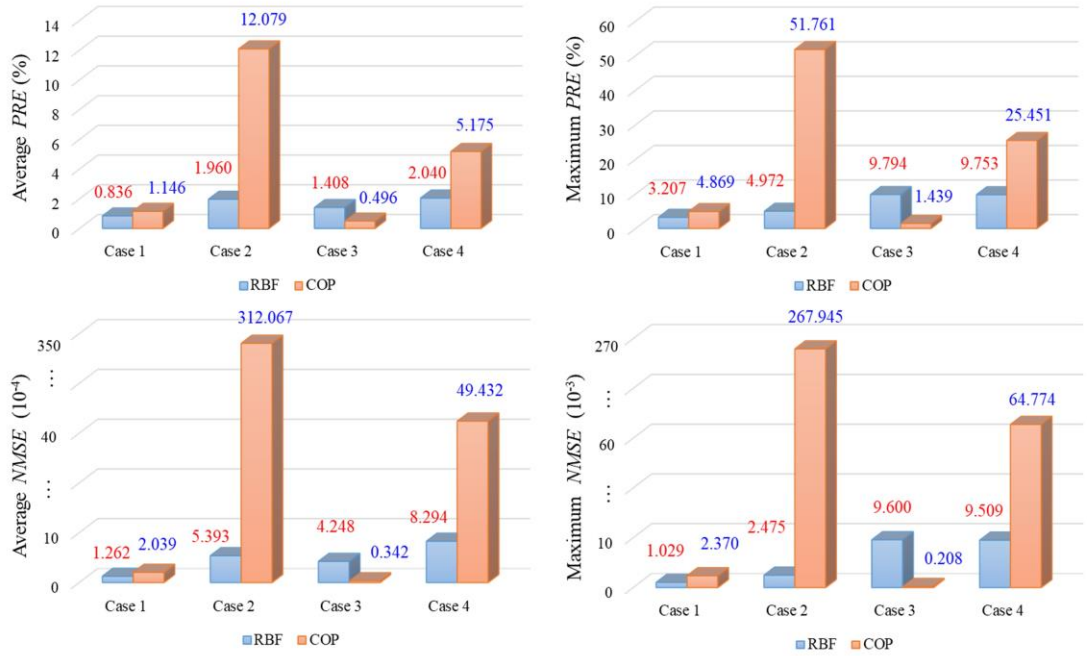

Fig. 13 The PRE and NMSE of deterministic identified DDL with different strategies

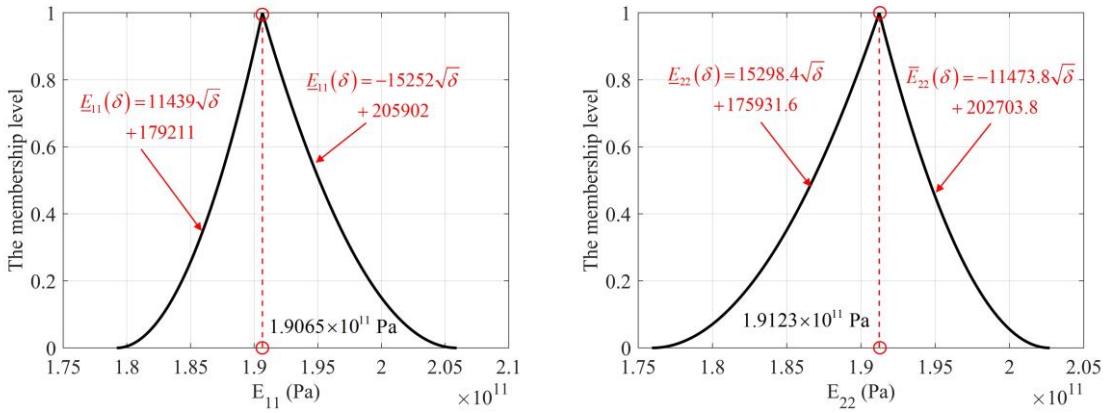

(a) Elasticity modulus E_{11} (b) Elasticity modulus E_{22}

Fig. 14 The description of fuzzy parameters

Particularly, 4 DDLs with different space-time distribution, as listed in Table 4, are involved to verify the generalization of the developed method. Moreover, the previous identification strategy with COPs [35] is also used to reconstruct the spatial distribution of DDLs. The reconstructed spatial load with the maximum amplitude in the time history (0.042s, 0.549s, 0.604s and 0.215s for cases 1 to 4), and the identified time histories of node 67 are summarized in Table 5. The average and maximum values of deterministic evaluation indexes (*PRE* and *NMSE*) for all FEM nodes are respectively presented in Fig. 13. What is surprising is that the identified loads by RBF approximation (load by RBF) can basically match the actual loads for 4 cases. The average *PREs* are less than 2.5% and the average *NMSEs* are not more than 1×10^{-3}. By contrast, the identified results by COP approximation are too worse to accept for case 2 and case 4, but they are better than the identified DDLs by

RBF approximation for case 3 with complete linearization in space domain (average *PREs* is 0.496% and average *NMSE* is 3.42×10^{-5}). As pointed out in Ref. [35], the hierarchical-clustering-oriented RBF approximation method possesses better generalization ability. In addition, the identified loads by RBF are consistent with their actual tendency in time domain for 4 cases, suggesting the effectiveness of the inverse Newmark iteration.

Further, the elastic modulus E_{11}, E_{22} is supposed to be fuzzy parameters as plotted in Fig. 14. The shear modulus G_{23}, G_{31} is assumed as convex parameters with a correlation coefficient of 0.8. The radii are set as $G_{23}^{r}=7.116\times10^{8}$ Pa and $G_{31}^{r}=5.84\times10^{8}$ Pa. Performing the uncertain DDL identification at 0-cut fuzzy parameters for case 1, identified intervals in space domain at 0.042s and in time domain of node 67 are exhibited in Fig. 15 (a) and (b) respectively. The load intervals can surround the actual forces perfectly, which shows the necessity of uncertainty propagation. And the fuzzy membership of the DDL at node 67 at 0.042s is plotted in Fig. 15 (c). Similar to the membership functions of elastic modulus E_{11} and E_{22}, the fuzzy membership functions of the concerned load are nearly linear when $\delta>0.4$, while nonlinear when $\delta<0.4$.

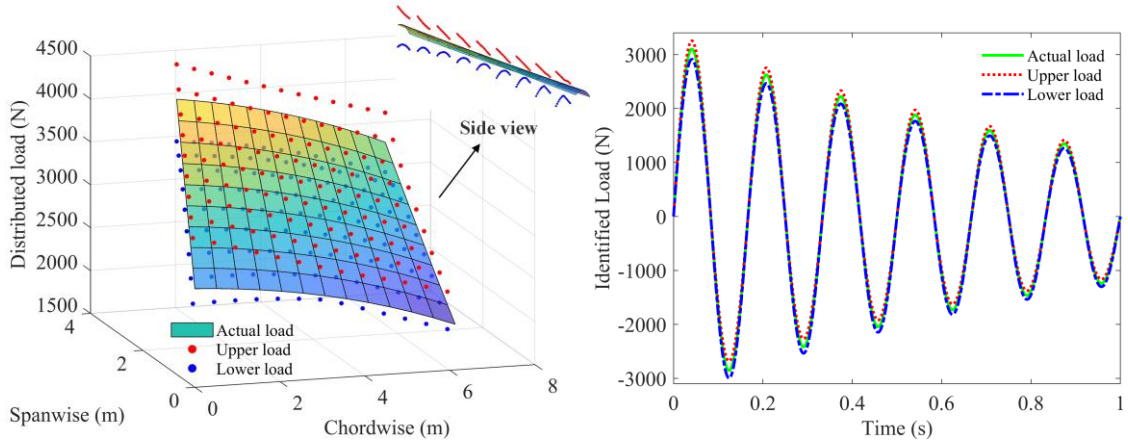

(a) In space domain (b) In time domain

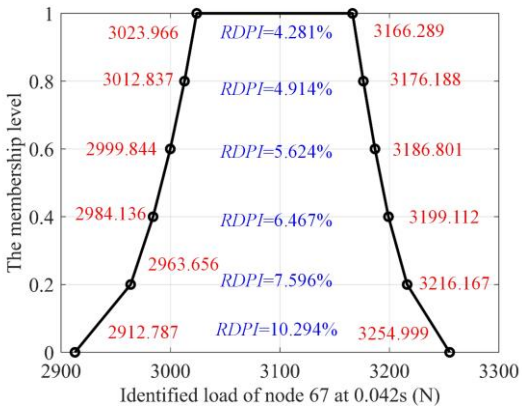

(c) Node 67 at 0.042s

Fig. 15 The identified DDL intervals for case 1

6.3 A wing structure

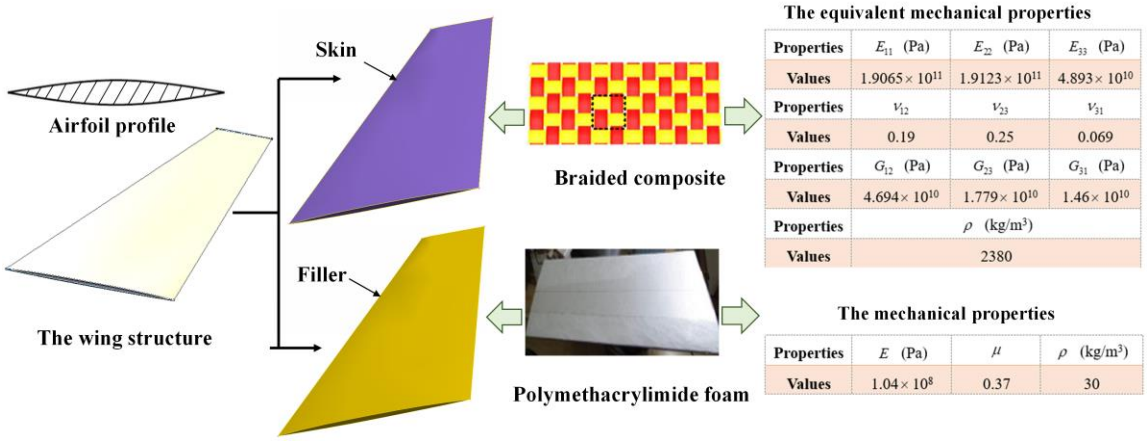

The equivalent mechanical properties

Properties	E_{11} (Pa)	E_{22} (Pa)	E_{33} (Pa)
Values	1.9065×10^{11}	1.9123×10^{11}	4.893×10^{10}
Properties	ν_{12}	ν_{23}	ν_{31}
Values	0.19	0.25	0.069
Properties	G_{12} (Pa)	G_{23} (Pa)	G_{31} (Pa)
Values	4.694×10^{10}	1.779×10^{10}	1.46×10^{10}
Properties	ρ (kg/m^3)		
Values	2380		

The mechanical properties

Properties	E (Pa)	μ	ρ (kg/m^3)
Values	1.04×10^{8}	0.37	30

(a) The geometric model

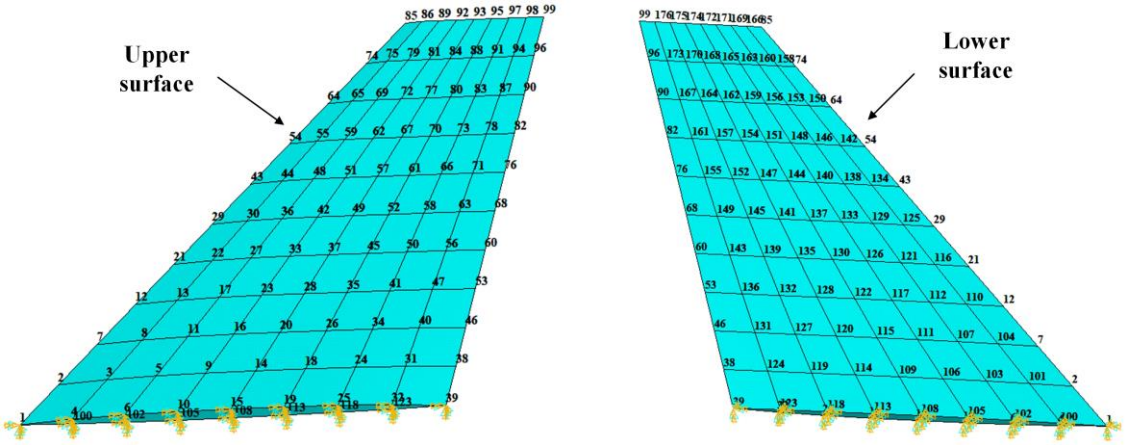

(b) The FEM model

Fig. 16 The three-dimensional wing structure

To better demonstrate the capability of the developed approach when dealing with complex engineering problems, a three-dimensional wing structure is further investigated. The wing structure is covered by the fiber fabric with a thickness of 0.2mm, and equivalent material parameters of the braided composite are obtained by parameter identification in both micro and macro scales. The interior is filled with isotropic polymethacrylimide foam. Fig. 16 (a) shows the geometric model and mechanical properties. By FEM discretization as shown in Fig. 16 (b), 224 nodes, 176 shell elements and 565 solid elements are generated. The coordinates are all regularized to a standard interval $\tilde{x},\tilde{y},\tilde{z}\in[-1,1]$. A DDL ($F=\left[50\tilde{x}^2+60\tilde{y}^2+30\tilde{z}+1120+20\ln(\tilde{z}+5t+8)+20(10-\tilde{x}+\tilde{y}+2t)^2\right]\left[\sin(16\pi t)-\sin(14\pi t)\right]$) is applied to the upper surface and lower surface, and the boundary condition is preset at the root of the wing structure.

Six different schemes of sensor placement (SP), as listed in Table 6, are provided in this example. Parametric studies of the proportional coefficient τ and overlap coefficient λ are explored in sequence to arrive at optimal RBF space based on the control variable method. The findings are listed in Table 7 and Table 8, followed by some conclusions as below.

Table 6 Different schemes of sensor placement

Sensor placement	**Node number**
1	40,44,87,103,149,158
2	3,63,75,121,124,164
3	5,28,58,59,88,107,119,130,147,158
4	3,30,35,67,84,107,124,130,149,160
5	3,28,31,36,66,69,94,106,121,127,138,145,157,158
6	5,31,17,47,49,67,85,101,115,136,137,150,152,173

Table 7 Parameter selection of proportional coefficient τ with $\lambda = 3$

Sensor placement		**1**	**2**	**3**	**4**	**5**	**6**
Average *PRE* (%)	τ=0.1	2.832	2.615	2.721	2.898	2.598	2.676
	τ=0.2	**1.739**	**1.651**	**1.282**	**1.709**	**1.411**	**1.290**
	τ=0.3	1.884	2.049	1.479	1.848	1.757	1.596
	τ=0.4	2.035	1.917	1.792	1.991	1.785	1.708
	τ=0.5	1.780	2.323	1.305	1.745	1.872	1.606
	τ=0.6	38.842	12.548	15.774	34.841	2.293	3.167
Average *NMSE* (10^{-4})	τ=0.1	18.481	18.717	17.959	18.919	17.984	17.771
	τ=0.2	**7.212**	**5.464**	**4.473**	**7.270**	**4.222**	**3.897**
	τ=0.3	8.301	7.726	4.909	8.539	5.337	4.634
	τ=0.4	8.977	6.622	6.129	9.414	5.458	5.157
	τ=0.5	7.295	9.958	3.945	7.405	6.009	4.641
	τ=0.6	2529.235	270.915	420.348	2041.501	9.093	17.572

Table 8 Parameter selection of proportional coefficient λ with optimal τ

Sensor placement		**1**	**2**	**3**	**4**	**5**	**6**
Average *PRE* (%)	$\lambda = 1$	1.824	2.371	2.317	2.481	2.288	2.283
	$\lambda = 2$	1.805	1.908	1.655	1.875	1.719	1.628
	$\lambda = 3$	**1.739**	**1.651**	**1.282**	**1.709**	**1.411**	**1.290**
	$\lambda = 4$	1.918	1.813	1.443	1.809	1.568	1.481
	$\lambda = 5$	1.922	1.955	1.563	1.865	1.722	1.607
	$\lambda = 6$	1.892	2.027	1.611	1.895	1.791	1.661
	$\lambda = 10$	1.736	2.152	1.567	1.869	1.855	1.685
Average *NMSE* (10^{-4})	$\lambda = 1$	6.776	13.459	11.385	11.753	12.281	11.502
	$\lambda = 2$	7.656	9.346	7.465	8.656	8.076	7.341
	$\lambda = 3$	**7.212**	**5.464**	**4.473**	**7.270**	**4.222**	**3.897**
	$\lambda = 4$	8.527	6.024	4.637	7.851	4.446	4.113
	$\lambda = 5$	8.449	6.996	5.081	8.322	5.133	4.656
	$\lambda = 6$	8.065	7.567	5.286	8.561	5.508	4.923
	$\lambda = 10$	6.862	8.574	5.058	8.285	5.901	5.027

(1) When the proportional coefficient τ is taken as 0.1, 0.2, 0.3, 0.4 0.5 and 0.6, the number of clusters is 121, 48, 22, 11, 7 and 3, respectively. Under the premise of $\lambda = 3$ (other values can be also selected), the average evaluation indexes (*PRE* and *NMSE*) of all FEM nodes are summarized in Table 7. Surprisingly, their minimums (which are bold) can be obtained for all schemes of SP when τ=0.2. And the centers' number is so small that the approximation ability of RBF is poor for the SP 1, 2, 3 and 4 when τ=0.6. A possible explanation is that the generated RBF space is relatively smooth, which is difficult to reflect the complicated mapping relationship between load distributions and node coordinates.

(2) The overlap coefficient λ controlling the width of RBF is investigated on the basis of $\tau = 0.2$. The results of average *PRE* and average *NMSE* under different schemes are listed in Table 8. We conclude that λ has little effect on the approximation ability of RBF. The evaluation indexes reach the bold minimum when $\lambda = 3$ for all schemes of SP.

(3) In summary, the hyper-parameters of RBF are uniquely determined for a given FEM model no matter how the sensor system is arranged. With the best parameters of $\tau = 0.2$ and $\lambda = 3$, the average *PRE* is less than 2%, and the average *NMSE* is less than 8×10^{-4}. The identified results are relatively superior for SP 3 and SP 6, which will be detailed below.

For the FEM nodes on the upper and lower surface, the cloud atlas of actual loads, identified loads and *PREs* in space domain at 0.534s (maximum load in the time history) are demonstrated in Fig. 17. Most *PRE*s are within 4% under the two SP schemes. The *PRE*s are relatively large in the root position nearby the front edge due to the influence of the boundary effects. And the maximum *PRE* (node 2) is 8.83% for SP3 and 7.98% for SP 6, which are acceptable for a complex wing structure. Besides, we can further increase the number of accelerometers or optimize the schemes of SP to improve the precision of DDL identification.

Taking the uncertainties into account, the elastic modulus E of polymethacrylimide foam is regarded as the fuzzy parameter, whose interval is assumed as $[0.988, 1.092] \times 10^8$ at its 0-cut level. The elastic modulus E_{11} and E_{22} in the main direction of the braided composite are considered as convex parameters with a correlation coefficient of 0.5. The radii are $E_{11}^r = 9.5325 \times 10^9$ Pa and $E_{22}^r = 9.5615 \times 10^9$ Pa. The cloud atlas of upper loads, lower loads and the *RDPIs* in time domain at 0.534s are plotted in Fig. 18. It can be seen that the distribution trend of the upper/lower bound is different from the actual load for both the upper and lower surface. The average *RDPI* of FEM nodes is 15.454%, and the *RDPI*s are relatively large at the root part of the wing structure. Eventually, the identified DDL at the nominal parameter and the load intervals in time domain of node 85 (maximum load of all FEM nodes) are shown in Fig. 19. Identical conclusions can be drawn as examples 1 and 2.

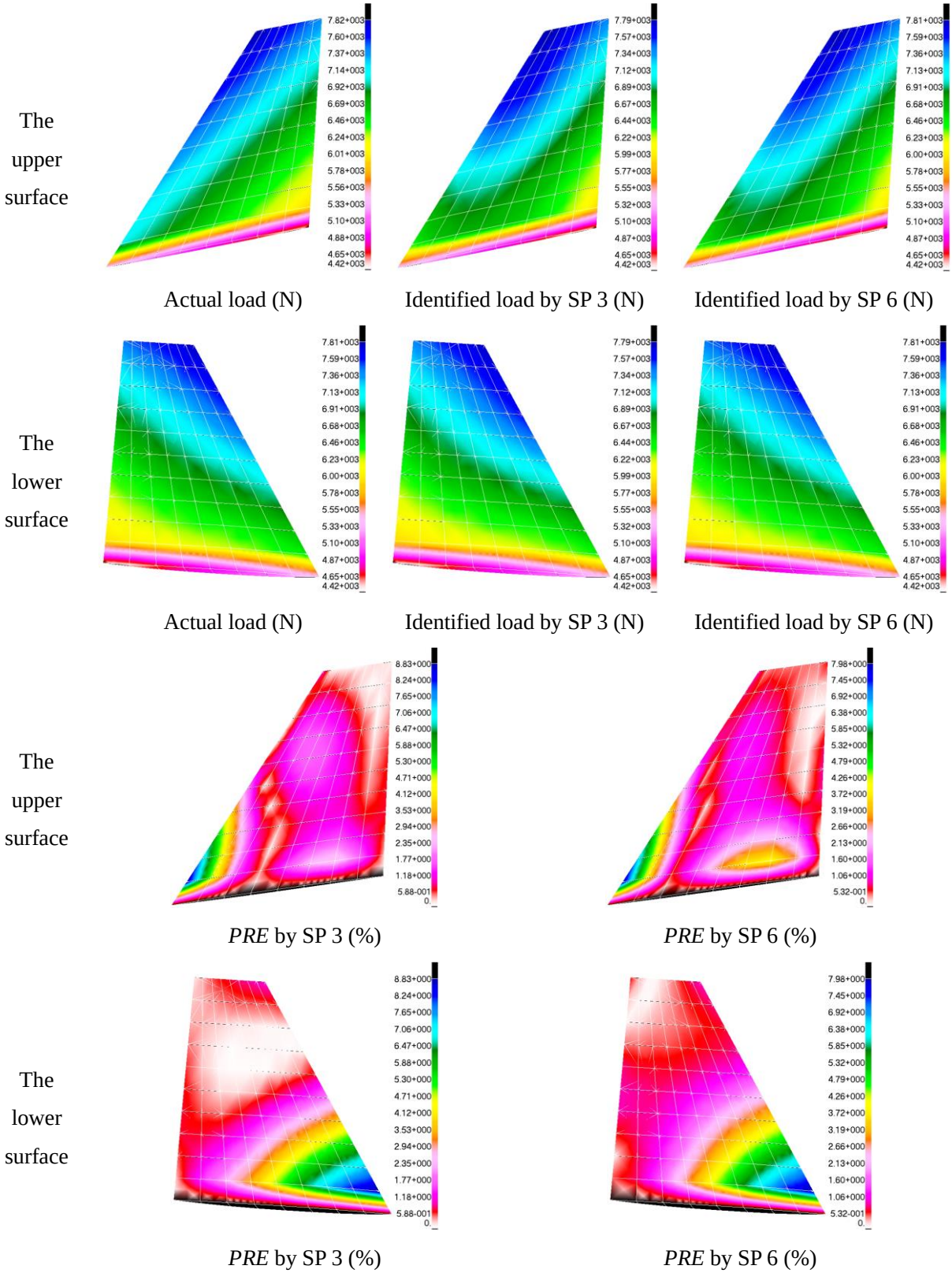

Fig. 17 The deterministic identified results in space domain

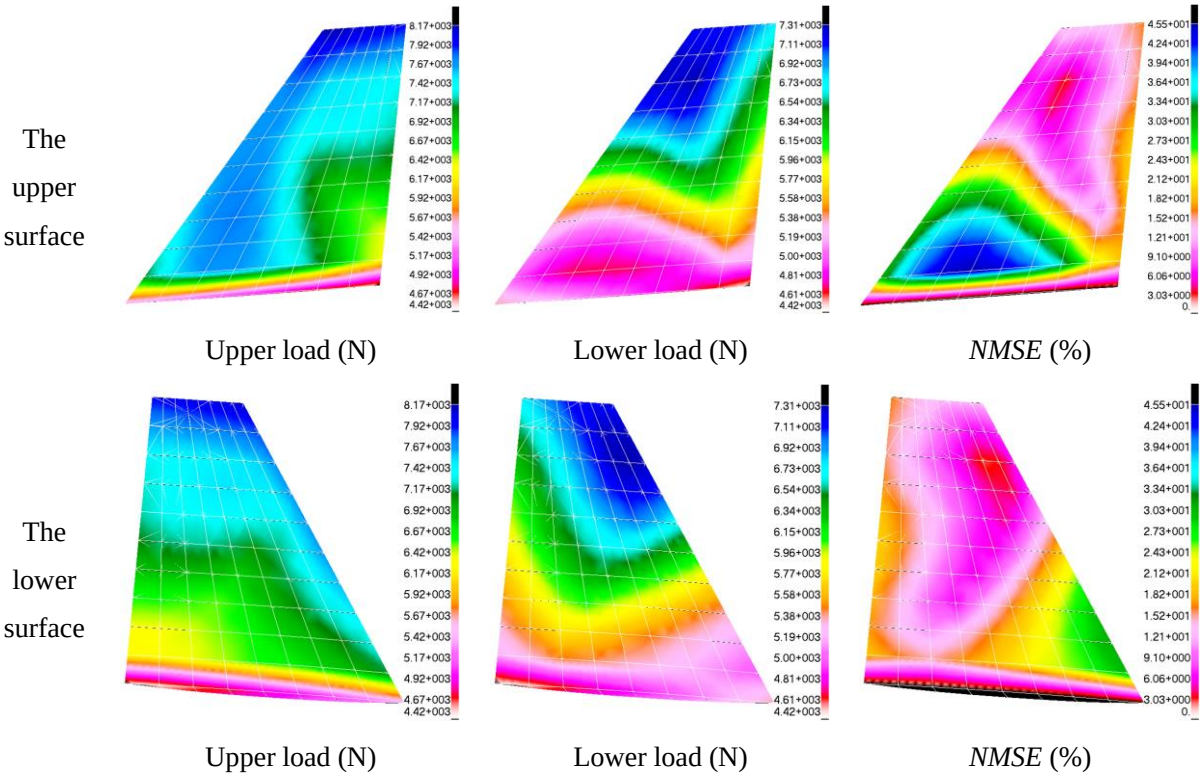

Fig. 18 The uncertain identified results in space domain

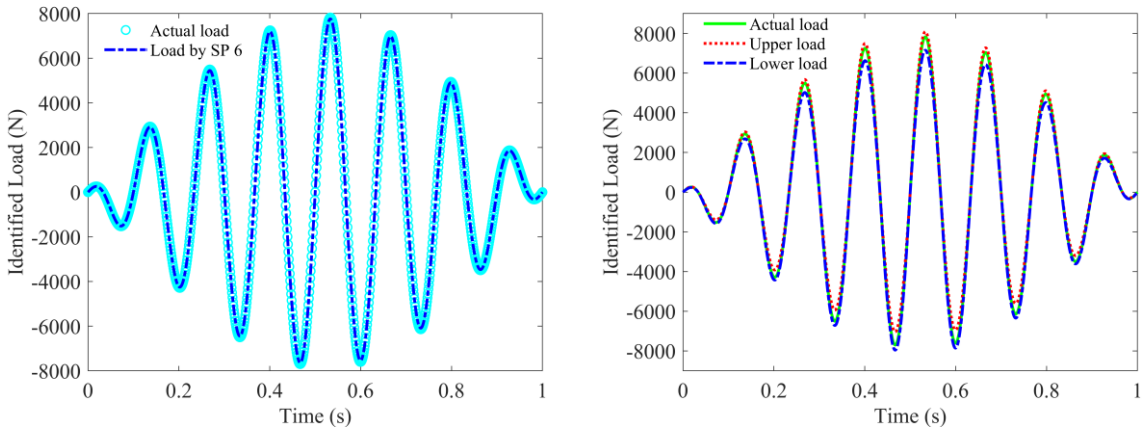

(a) At the nominal parameter (b) Load boundaries

Fig. 19 The identified results in time domain of node 85

7 Conclusions

As revealed by the above issues, a novel spatio-temporal DDL identification method using limited acceleration measurements considering convex-fuzzy hybrid uncertainties is developed for proportionally damped systems, which combines the dynamic inverse, RBF approximation and uncertainty treatment. Major novelty contributions lie in that: (1) The DDLs are decomposed by the hierarchical-clustering-oriented RBF approximation and time discreteness, which converts the DDL identification to the calculation of RBF coefficients at

every sampling instant. (2) The hybrid convex-fuzzy uncertainties are uniformly characterized by a multi-dimensional interval model through space transformation and membership truncation. (3) The Chebyshev-interval collocation method is proposed to effectively achieve the fuzzy interval bounds of the DDLs through uncertain dynamics evolution. Numerical examples demonstrate the effectiveness of the presented methodology (including uncertain propagation and DDL approximation), and they also show that the sensor deployments and RBF parameters both have great influences on the identified results.

Acknowledgments

The authors would like to thank the National Nature Science Foundation of China (12072007, 12072006), the EU Marie Sklodowska-Curie Individual Fellowships (H2020-MSCA-IF-2020:101025743-ROFiDMS), the Defense Industrial Technology Development Program (JCKY2019203A003, JCKY2019205A006, JCKY2019209C004) and the Ningbo Nature Science Foundation (202003N4018). Besides, the authors wish to express their many thanks to the reviewers for their useful and constructive comments.

References

[1] J. Sanchez, H. Benaroya. Asymptotic approximation method of force reconstruction: Proof of concept[J], Mechanical Systems and Signal Processing. 2017, 92:39-63.

[2] L. Wang, Y.R. Liu, K.X. Gu, et al. A radial basis function artificial neural network (RBF ANN) based method for uncertain distributed force reconstruction considering signal noises and material dispersion[J], Computer Methods in Applied Mechanics and Engineering. 2020, 364:112954.

[3] H. Liu, Q.S. Liu, B. Liu, et al. An efficient and robust method for structural distributed load identification based on mesh superposition approach[J], Mechanical Systems and Signal Processing. 2021, 151:107383.

[4] Y.R. Liu, L. Wang, K.X. Gu. A support vector regression (SVR)-based method for dynamic load identification using heterogeneous responses under interval uncertainties[J], Applied Soft Computing. 2021:107599.

[5] Y.R. Liu, L. Wang, Z.P. Qiu, et al. A dynamic force reconstruction method based on modified kalman filter using acceleration responses under multi-source uncertain samples[J], Mechanical Systems and Signal Processing. 2021.

[6] L. Wang, Y.R. Liu, Y.S. Liu. An inverse method for distributed dynamic load identification of structures with interval uncertainties[J], Advances in Engineering Software. 2019, 131:77-89.

[7] J. Liu, X. Han, K. Li, et al. A novel approach for distributed dynamic load reconstruction by space-time domain decoupling[J], Journal of Sound and Vibration. 2015, 348:137-148.

[8] L. Yi, W.S. Shepard. An improved method for the reconstruction of a distributed force acting on a vibrating structure[J], Journal of Sound and Vibration. 2006, 291 (1):369-387.

[9] C.W. Coates, P. Thamburaj. Inverse method using finite strain measurements to determine flight load distribution functions[J], Journal of Aircraft. 2008, 45 (2):366-370.

[10] S. Granger, L. Perotin. An inverse method for the identification of a distributed random excitation acting on a vibrating structure part 1: theory[J], Mechanical Systems and Signal Processing. 1999, 13 (1):53-65.
[11] D. Dessi. Load field reconstruction with a combined POD and integral spline approximation technique[J], Mechanical Systems and Signal Processing. 2014, 46 (2):442-467.
[12] J. Liu, K. Li. Sparse identification of time-space coupled distributed dynamic load[J], Mechanical Systems and Signal Processing. 2021, 148:107177.
[13] R. Schaback. Error estimates and condition numbers for radial basis function interpolation[J], Advances in Computational Mathematics. 1995, 3 (3):251-264.
[14] J. Park, I. Sandberg. Universal approximation using radial-basis-function networks[J], Neural Computation. 2014, 3 (2):246-257.
[15] G.E. Fasshauer, M.J. Mccourt, Stable evaluation of Gaussian radial basis function interpolants[M], Stable Evaluation of Gaussian Radial Basis Function Interpolants, 2012.
[16] R. Savitha, S. Suresh, N. Sundararajan. A fully complex-valued radial basis function network and its learning algorithm[J], International Journal of Neural Systems. 2009, 19 (4):253-267.
[17] J. Wang, A. Belatreche, L. Maguire, et al. An online supervised learning method for spiking neural networks with adaptive structure[J], Neurocomputing. 2014, 144:526-536.
[18] S. Chen, C.F.N. Cowan, P.M. Grant. Orthogonal least squares learning algorithm for radial basis function networks[J], IEEE Trans Neural Networks. 1991, 2 (2):302-309.
[19] L. Wang, Y.R. Liu, D.L. Liu, et al. A novel dynamic reliability-based topology optimization (DRBTO) framework for continuum structures via interval-process collocation and the first-passage theories[J], Computer Methods in Applied Mechanics and Engineering. 2021, 386:114107.
[20] C. Jiang, J. Zheng, X. Han. Probability-interval hybrid uncertainty analysis for structures with both aleatory and epistemic uncertainties: a review[J], Structural and Multidiplinary Optimization. 2018, 67 (6):2485-2502.
[21] A.K. Prasad, S. Roy. Reduced dimensional Chebyshev-Polynomial chaos aproach for fast mixed epistemic-aleatory uncertainty quantification of transmission line networks[J], IEEE Transactions on Components, Packaging, and Manufacturing Technology. 2018, 9 (6):1119-1132.
[22] H. Yin, D.J. Yu, S.W. Yin, et al. Fuzzy interval Finite Element/Statistical Energy Analysis for mid-frequency analysis of built-up systems with mixed fuzzy and interval parameters[J], Journal of Sound and Vibration. 2016, 380:192-212.
[23] A. DMD, G.B. Kang, Y.C. Wei, et al. Hybrid uncertainty analysis of functionally graded plates via multiple-imprecise-random-field modelling of uncertain material properties[J], Computer Methods in Applied Mechanics and Engineering. 2020, 368:113116.
[24] S.M. Mousavi, B. Vahdani, R. Tavakkoli-Moghaddam, et al. Location of cross-docking centers and vehicle routing scheduling under uncertainty: A fuzzy possibilistic–stochastic programming model[J], Applied Mathematical Modelling. 2014, 38 (7):2249-2264.
[25] B.F. Dong, Z.Z. Lu. An efficient estimation of failure probability in the presence of random and interval hybrid uncertainty[J], Structural and Multidiplinary Optimization. 2021:1-23.
[26] L. Meirovitch, Principles and Techniques of Vibrations[M], Principles and Techniques of Vibrations, 1997.
[27] A.K. Jain. Data clustering: 50 years beyond K-means[J], Pattern Recognition Letters. 2010, 31 (8):651-666.
[28] T. Sørlie, C.M. Perou, R. Tibshirani, et al. Gene expression patterns of breast carcinomas distinguish tumor subclasses with clinical implications[J], Proceedings of the National Academy of Sciences. 2001, 98 (19):10869-10874.
[29] C.C. Astuti, R.S. Untari. Applied hierarchical cluster analysis with average linkage algoritm[J], CAUCHY. 2017, 5 (1):1-7.

[30] Y.R. Liu, L. Wang, K.X. Gu, et al. Artificial Neural Network (ANN) - Bayesian Probability Framework (BPF) based method of dynamic force reconstruction under multi-source uncertainties[J], Knowledge-Based Systems. 2021:107796.

[31] C. Jiang, X. Han, G.Y. Lu, et al. Correlation analysis of non-probabilistic convex model and corresponding structural reliability technique[J], Computer Methods in Applied Mechanics and Engineering. 2011, 200 (33-36):2528-2546.

[32] C.C. Yang, N.K. Bose. Generating fuzzy membership function with self-organizing feature map[J], Pattern Recognition Letters. 2006, 27 (5):356-365.

[33] J.L. Wu, Z. Luo, N. Zhang, et al. A new uncertain analysis method and its application in vehicle dynamics[J], Mechanical Systems and Signal Processing. 2015, 50:659-675.

[34] J.L. Wu, Y.Q. Zhang, L.P. Chen, et al. A Chebyshev interval method for nonlinear dynamic systems under uncertainty[J], Applied Mathematical Modelling. 2013, 37 (6):4578-4591.

[35] L. Wang, Y.R. Liu. A novel method of distributed dynamic load identification for aircraft structure considering multi-source uncertainties[J], Structural and Multidiplinary Optimization. 2020, 61 (5):1929-1952.